



**HAL**  
open science

## **A multiscale mathematical model of cell dynamics during neurogenesis in the mouse cerebral cortex**

Marie Postel, Alice Karam, Guillaume Pézeron, Sylvie Schneider-Maunoury, Frédérique Clément

► **To cite this version:**

Marie Postel, Alice Karam, Guillaume Pézeron, Sylvie Schneider-Maunoury, Frédérique Clément. A multiscale mathematical model of cell dynamics during neurogenesis in the mouse cerebral cortex. 2018. hal-01783141v1

**HAL Id: hal-01783141**

**<https://inria.hal.science/hal-01783141v1>**

Preprint submitted on 2 May 2018 (v1), last revised 17 Sep 2019 (v2)

**HAL** is a multi-disciplinary open access archive for the deposit and dissemination of scientific research documents, whether they are published or not. The documents may come from teaching and research institutions in France or abroad, or from public or private research centers.

L'archive ouverte pluridisciplinaire **HAL**, est destinée au dépôt et à la diffusion de documents scientifiques de niveau recherche, publiés ou non, émanant des établissements d'enseignement et de recherche français ou étrangers, des laboratoires publics ou privés.

# A MULTISCALE MATHEMATICAL MODEL OF CELL DYNAMICS DURING NEUROGENESIS IN THE MOUSE CEREBRAL CORTEX

Postel Marie<sup>1\*\*</sup>, Karam Alice<sup>2\*</sup>, Pézeron Guillaume<sup>2°</sup>, Schneider-Maunoury Sylvie<sup>2‡\*</sup>, Clément Frédérique<sup>3,4‡</sup>

**1 Sorbonne Université, Université Paris-Diderot SPC, CNRS, Laboratoire Jacques-Louis Lions, LJLL, F-75005 Paris**

**2 Sorbonne Université, CNRS UMR7622, Inserm U1156, Institut de Biologie Paris-Seine (IBPS), Laboratoire de Biologie du développement (LBD), F-75005, Paris**

**3 Inria, Université Paris-Saclay**

**4 LMS, Ecole Polytechnique, CNRS, Université Paris-Saclay**

**\* These authors contributed equally to this work.**

**‡These authors also contributed equally to this work.**

**° Current address: CNRS-UMR7221, Muséum National d'Histoire Naturelle, Sorbonne Université, Paris, France**

**\* Authors for correspondance: Marie.Postel@sorbonne-universite.fr;  
sylvie.schneider-maunoury@sorbonne-universite.fr**

## 1 Abstract

Neurogenesis in the murine cerebral cortex involves the coordinated divisions of two main types of progenitor cells, whose numbers, division modes and cell cycle durations set up the final neuronal output. To understand the respective roles of these factors in the neurogenesis process, we combine experimental in vivo studies with mathematical modeling and numerical simulations of the dynamics of neural progenitor cells. A special focus is put on the population of intermediate progenitors (IPs), a transit amplifying progenitor type critically involved in the size of the final neuron pool. A multiscale formalism describing IP dynamics allows one to track the progression of cells along the subsequent phases of the cell cycle, as well as the temporal evolution of the different cell numbers. Our model takes into account the dividing apical progenitors (AP) engaged into neurogenesis, both neurogenic and proliferative IPs, and the newborn neurons. The transfer rates from one population to another are subject to the mode of division (symmetric, asymmetric, neurogenic) and may be time-varying. The model outputs are successfully fitted to experimental cell numbers from mouse embryos at different stages of cortical development, taking into account IPs and neurons, in order to adjust the numerical parameters. Applying the model to a mouse mutant for *Ftm/Rprip1l*, a gene involved in human ciliopathies with severe brain abnormalities, reveals a shortening of the neurogenic period associated with an increased influx of newborn IPs from apical progenitors at mid-neurogenesis. Additional information is provided on cell kinetics, such as the mitotic and S phase indexes, and neurogenic fraction. Our model can be used to study other mouse mutants with cortical neurogenesis defects and can be adapted to study the importance of progenitor dynamics in cortical evolution and human diseases.

## 2 Introduction

The multiple functions of the mammalian cerebral cortex in integrating sensory stimuli, controlling motor output and mediating cognitive functions are supported by an extraordinary diversity of neuronal subtypes mutually connected through complex neuronal circuitry. The formation of this structure requires producing the correct numbers and subtypes of neurons at the proper position during a specific period

of embryonic and fetal development, the neurogenesis period, which lasts a few days in mice to a few months in humans [14, 22, 27].

The cerebral cortex is a laminar structure in the dorsal telencephalon, composed of two major classes of neurons, pyramidal neurons and interneurons. We focus on pyramidal neurons, which are more abundant and, unlike interneurons, are generated by local progenitors in the dorsal telencephalon. Apical progenitors (APs) in the cortical ventricular zone (VZ) give birth to populations of basal progenitors (BPs) forming the subventricular zone (SVZ), mainly populated in the mouse cortex with intermediate progenitors (IPs) [26, 28]. Cortical progenitors display distinct modes of division (illustrated in Fig 2 for the mouse cortex) [27] and cell cycle parameters [1]. Before the onset of neurogenesis in mouse embryos, APs divide symmetrically to expand the progenitor pool. At the onset of neurogenesis, APs start to divide asymmetrically to self-renew and produce either one neuron (direct neurogenesis) or one IP that migrates into the SVZ. IPs divide symmetrically, once or possibly twice, leading to the production of either two or four neurons. Neurogenic IPs (IPNs) give birth to two neurons directly after one cell cycle. Proliferative IPs (IPPs) give birth to two neurogenic IPs, each of which will in turn give rise to two neurons. Young neurons then migrate radially toward the cortical plate [3, 16, 26, 28].

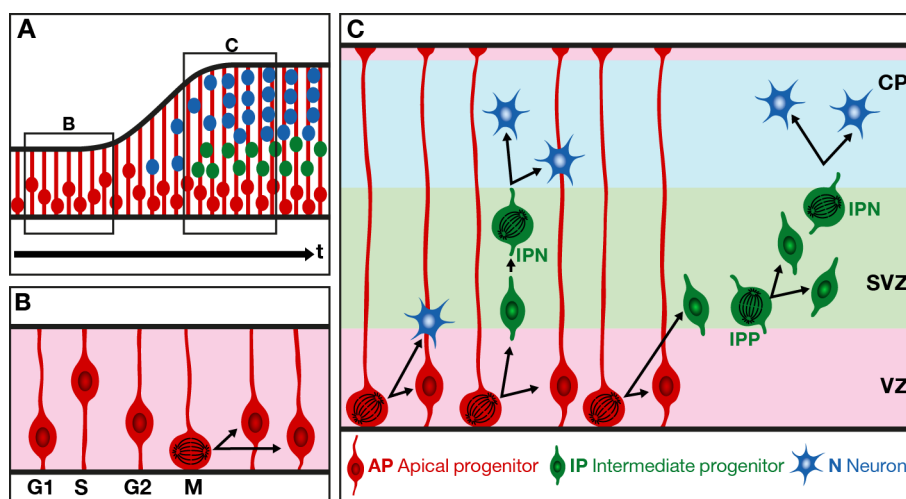


Figure 1: Schematic representation of cortical neurogenesis during mouse brain development. Dividing apical progenitor nuclei undergo interkinetic nuclear migration (INM): their nuclei move within the ventricular zone, from the apical surface toward basal (G1-S phases) then back to the apical surface (S-G2 phases) where they divide (M phase). A) Representation of the cortex at different developmental stages. The black arrow represents developmental time. Boxed areas B and C correspond to stages before neurogenesis and during neurogenesis, respectively. B) Before the onset of neurogenesis, APs divide symmetrically to give rise to two new APs, leading to an expansion of the AP population and consequently of the ventricular surface. C) From the onset of neurogenesis (E12.5) until the end of gestation (E18.5), APs divide asymmetrically to self-renew and to give rise to a neuron that migrates toward the cortical plate (CP) (direct neurogenesis) or to an IP (IP-genic division) that migrates out of the ventricular zone (VZ) to form the subventricular zone (SVZ). IPs can either be IPNs that divide to give rise to 2 neurons or IPPs that divide to give rise to two IPNs.

Many factors contribute to the dynamics of neurogenesis and to the final neuronal number: the timing of initiation and termination of neurogenesis, the initial number of apical progenitors, the ratio of each division type, the duration of the cell cycles. Moreover, in pathological contexts, several factors may be modified simultaneously, complicating the interpretation. The current study was motivated by the observation of complex cortical neurogenesis defects in a mouse knock-out mutant for the *Ftm/Rpgrip1l* gene (hereafter called the *Ftm* mutant). The *Ftm/Rpgrip1l* gene encodes a protein involved in the formation and function of the primary cilium [6, 9, 32], a sensory organelle projecting from the cell surface with multiple functions in development and whose defects cause human syndromes called ciliopathies [5] [18]. At the peak of cortical neurogenesis (around embryonic stage E14.5), *Ftm*<sup>-/-</sup> fetuses show a strong

reduction in the numbers of neurons and IPs. Intriguingly, at later stages the neurogenesis defect is at least partly compensated for.

In this work, we explore further whether this compensation may be due to differences in the neurogenic potential of APs and IPs, and/or in the proliferation potential of IPs, and especially in the proportion of IPs undergoing two consecutive cell cycles (IPgenic IPs, IPPs) instead of one (neurogenic IPs, IPNs). Additionally, we set up a framework in which one can study the impact of the durations of the whole cell cycle and of any of the cell cycle phases. We aim to quantify the impact on the final neuronal output of changes in progenitor proliferation/neurogenesis rates at different developmental stages, to interpret our mutant phenotypes and possibly to guide future experiments.

We combine an experimental quantitative *in vivo* investigation of the different cell types along the whole neurogenesis process with the design of a mathematical model for cell population dynamics, which is derived from cell-kinetics principles and based on a deterministic, spatio-temporal formalism. Numerical simulations of our model allows one to follow the numbers of (i) dividing APs committed to neurogenesis, (ii) newborn neurons, and (iii) neurogenic and IPgenic IPs. The transfer rates from one population to another are subject to the type of division and may be time-varying.

The simulated cell numbers are fitted to the experimental numbers to calibrate the parameters entering the formulations of the transfer rates. In the case of (either neurogenic or IPgenic) IPs, one can also follow the progression along the subsequent phases of the cell cycle (G1, S, G2, M). Additional biological outputs related to IPs are thus available, such as the mitotic index (MI) and labeling index (LI, also called S-phase index), as well as MI- or LI- derived information (e.g. the fraction of neurogenic mitoses). The computation of such outputs also enables us to illustrate how the model can be used to supply computer-assisted help in the design and assessment of experimental protocols devoted to cell kinetics analysis.

As detailed in the discussion, modeling approaches of cell lineage dynamics have been mainly undertaken in the framework of the branching process formalism applied to embryonic [13, 21, 24, 30] or adult [20] neurogenesis. The natural time increment is expressed as the cell generation number, which can hardly be matched to embryonic days. The real temporal dynamics of progenitor cells have been rather investigated in either stochastic [12] or deterministic [35, 36] compartmental models, yet without considering the structuring of the cell cycle into different phases.

To our knowledge, our results provide the first quantitative and dynamic cell-based description of brain cortex development. We describe the quantitative changes in the AP, IP and neuron populations during the whole neurogenesis period in mice. From information on global cell numbers, we can derive information on the rate and mode of cell divisions underlying the neural lineage, and track in an accurate way the progression of IPs along the cell cycle. Comparisons of the results obtained from the wild-type and *Ftm* mutant mice suggest that a major effect of the *Ftm* mutation is to shorten the duration of the neurogenic period, which appears to start later, while it ends up at a similar time with an only slightly reduced neuronal yield. Together with the neurogenesis shortening, the compensation for neuron production requires an intensive recruitment of committed APs at mid-neurogenesis, where the IP numbers exhibit a narrow high-amplitude peak. Our modeling approach, based on data-driven outputs, allows us to monitor the time course of IP progenitors and neurogenic AP inflow in both control and mutant situations.

## 3 Results

### 3.1 Design of the mathematical model and model outputs

The model investigates the neurogenesis steps occurring from the initiation of AP engagement in neurogenesis (hence the apparition of neurogenic or IPgenic divisions of APs) until neurogenesis ending (which corresponds to a switch to gliogenesis in normal conditions [25, 31]).

#### 3.1.1 General framework

The general structure of the model is based on a deterministic compartmental model with 4 compartments : an inflow compartment corresponding to APs engaged in neurogenesis, an outflow compartment

corresponding to neurons, and in between, the compartments corresponding to proliferative and neurogenic IPs.

The instantaneous inflow of APs, denoted by  $F_{AP}(t)$  (Fig. 3.1.1) is distributed amongst three cell types according to possibly time-varying rates. APs engaged in neurogenesis can either undergo direct neurogenesis (transition  $AP \rightarrow N$ ) with rate  $(1-\beta(t))$  or give birth to intermediate progenitors with rate  $\beta(t)$ . The non neurogenic AP flow is further separated into:

- the production of neurogenic IPs (IPs that will complete a single cell cycle before engendering neurons through transition  $IPN \rightarrow N$ ) with rate  $\beta(t)(1-\gamma(t))$  (transition  $AP \rightarrow IPN$ );
- the production of IPgenic IPs (IPs that will complete two successive cell cycles and be at the source of IPNs at the end of their first cycle) with rate  $\beta(t)\gamma(t)$  (transition  $AP \rightarrow IPP$ ).

Hence, there are two incoming flows in the IPN compartment : one stemming from APs and another from IPPs.

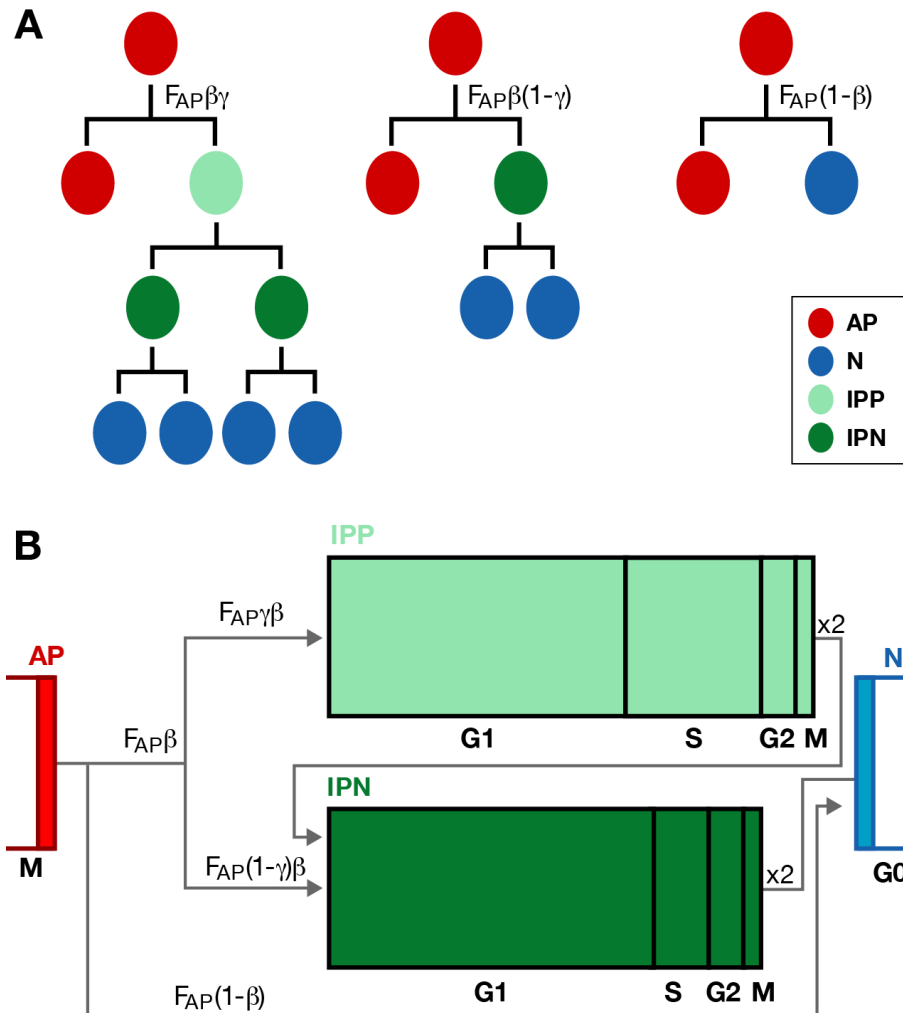


Figure 2: Modes of division of cortical progenitors and cell cycle phases. (A) Schematic diagram of the different modes of neural progenitor cell divisions (B) Another representation of progenitor divisions highlighting the duration of the cell cycle phases according to [1]. Note the difference in the duration of phases G1 and S in IPPs as compared to IPNs.

Embedded within this compartment structure, the dynamics of IP cell populations are described in more details and encompass several scales.

### 3.1.2 Local (microscopic) scale

The model describes the progression along the cell cycle and the repartition into the different cell cycle phases of the intermediate progenitors through their local cell densities  $IPP(t, a)$  and  $IPN(t, a)$ . The first variable  $t$  denotes the time, measured in embryonic days, and the second variable  $a$  is the cytological age (i.e. the time elapsed since last mitosis), measured in hours.

The evolution of the cell densities  $X(t, a) = IPP(t, a)$  or  $X(t, a) = IPN(t, a)$  is the outcome of a linear non conservative transport equation with unit speed for  $a \in ]0, T_C^X[$

$$\begin{cases} \partial_t X(t, a) + \partial_a X(t, a) = 0, & t > 0, \\ X(0, a) = X_0(a), \end{cases} \quad (1)$$

where  $T_C^X$ , the cell cycle duration, is the (constant) length of the domain, which differs between neurogenic and IPgenic IPs. System (1) is accompanied by proper boundary conditions representing the coupling between the different cell types: AP inflow into IPP or IPN, IPP inflow into IPN, and IPN outflow into N. We have

$$\begin{aligned} IPP(t, 0) &= \gamma(t)\beta(t)F_{AP}(t) \\ IPN(t, 0) &= (1 - \gamma(t))\beta(t)F_{AP}(t) + 2IPP(t, T_C^{IPP}) \end{aligned} \quad (2)$$

$$\frac{dN}{dt}(t) = (1 - \beta(\tau))F_{AP}(t) + 2IPN(t, T_C^{IPN}). \quad (3)$$

The coupling term (3) allows one to distinguish the contribution of direct neurogenesis from that of neurogenic IPs.

While the total length of the spatial domain corresponds to the cell cycle duration  $T_C^X$ , the locations of its internal boundaries correspond to the durations of the different cell cycle phases, which differ between neurogenic and IPgenic IPs:

$$T_C^X = T_{G1}^X + T_S^X + T_{G2}^X + T_M^X, \text{ where } X = IPP \text{ or } X = IPN$$

With specific choices of the  $\beta(t)$ ,  $\gamma(t)$  and  $F_{AP}(t)$  functions, equations (1-2) can be solved numerically using the method of characteristics (see Material & Methods). The 2D visualization in Fig 3.1.2 enables one to follow the changes in the distributions of IPPs (left panel) and IPNs (right panel). The horizontal axis corresponds to time, and the vertical axis to the cell age. The horizontal black lines mark the locations of inner boundaries delimiting the cell cycle (G1,S, G2 and M) phases, each having different durations in IPPs and IPNs. The same color code is used for both IPPs and IPNs. Neurogenesis starts a little before E12 and results in the appearance of newborn cells in both the IPP and IPN domains. At E17, the inflow from APs dries up and at E18, the last IPPs complete mitosis and enter the IPN compartment which, in turn, empties around E19.

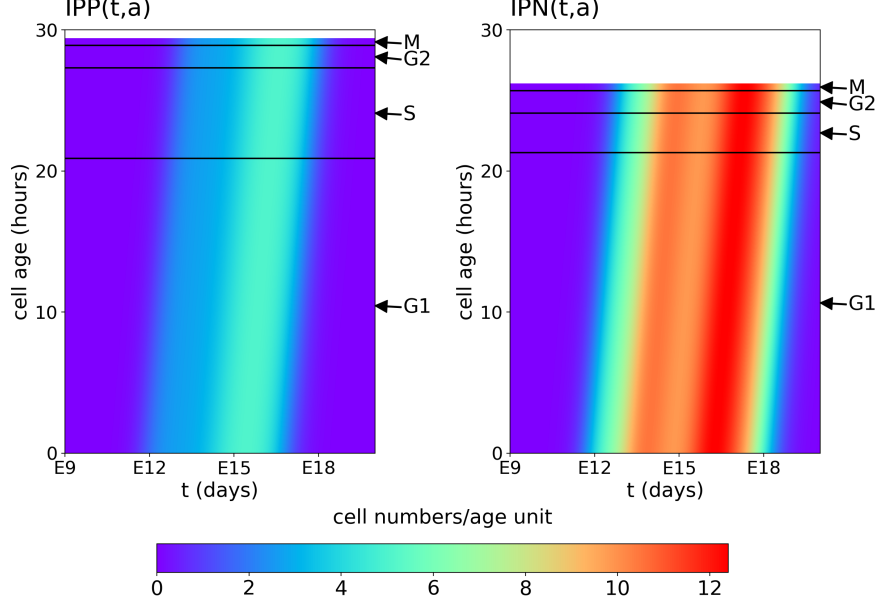


Figure 3: Display of the IPP and IPN cell densities in the age/time plane, computed using the model, for the parameter set 3 from Table 3.3.2. The black horizontal lines delineate the G1, S, G2, and M phases. The same color code is used for both IPPs and IPNs (number of cells per age unit). The horizontal axis corresponds to the time, and the vertical axis to the age of the cells within the cell cycle. The horizontal black lines indicates the different phases, which have different durations for IPP and IPN (see S2 Table).

### 3.1.3 Global (macroscopic) scale

For any cell type ( $X = IP, IPP, IPN$  or  $N$ ), we can compute the cell number as a function of time, which we denote  $\bar{X}(t)$ .

For IPP and IPN cell we can compute the number of cells at a given time by integrating the age distribution over the whole cell cycle duration ( $T_C^{IPP}$  or  $T_C^{IPN}$ )

$$\begin{aligned}\overline{IPP}(t) &= \int_0^{T_C^{IPP}} IPP(t, a) da, \\ \overline{IPN}(t) &= \int_0^{T_C^{IPN}} IPN(t, a) da,\end{aligned}\tag{4}$$

from which we can compute the total number of IP cells

$$\overline{IP}(t) = \overline{IPP}(t) + \overline{IPN}(t).\tag{5}$$

The number of neurons at a given time  $N(t)$  is obtained directly from integrating (3) in time

$$N(t) = \int_0^t ((1 - \beta(\tau))F_{AP}(\tau) + 2IPN(\tau, T_C^{IPN})) d\tau.\tag{6}$$

### 3.1.4 Semi-global(mesoscopic) scale

In the case of IPs and IPNs, we can compute partial cell numbers within each phase of the cell cycle, and especially phases S and M, so that we can also derive expressions for the mitotic (MI) and labeling (LI)

indexes in the IP population. For  $X = IPP$  or  $X = IPN$  we obtain

$$\begin{aligned}\bar{X}_S(t) &= \int_{T_{G_1}^X}^{T_{G_1}^X + T_S^X} X(t, a) da, \\ \bar{X}_M(t) &= \int_{T_{G_1}^X + T_S^X + T_{G_2}^X}^{T_c^X} X(t, a) da,\end{aligned}\tag{7}$$

hence

$$LI(t) = \frac{\overline{IPP}_S(t) + \overline{IPN}_S(t)}{\overline{IP}(t)},\tag{8}$$

$$MI(t) = \frac{\overline{IPP}_M(t) + \overline{IPN}_M(t)}{\overline{IP}(t)}.\tag{9}$$

We emphasize that such indexes follow quite complex temporal patterns as soon as one deviates from the ideal situation of a population of self-renewing asynchronous cells distributed uniformly along the cell cycle. In this ideal case, the mitotic index is a constant and can be accurately estimated from the relative duration of the mitosis with respect to the whole cycle duration. Even in the still simple case of an exponentially growing cell population, the MI is subject to periodic fluctuations (with a period equaling the cell cycle duration) and the relation between the MI and the relative M phase duration becomes loglinear. Things get rapidly more complicated and intuitively unpredictable when one accounts for events leading to cell cycle exit (due for instance to quiescence, apoptosis or terminal differentiation). We refer the interested reader to the thorough study performed in [4] on the MI dynamic pattern.

To sum up, the IP dynamics spans three scales:

- Cell densities  $IPP(t, a)$  and  $IPN(t, a)$  are defined on the lowest (local) level;
- Partial cell numbers  $\bar{X}_P(t)$  (with  $X \in \{IPP, IPN, IP\}$  and  $P \in \{G1, S, G2, M\}$ ), and the related cell kinetics indexes are defined on the intermediate (semi-local) level;
- Whole cell numbers  $\overline{IPP}(t), \overline{IPN}(t)$  and  $\overline{IP}(t)$  are defined on the highest (global) level.

### 3.2 Acquisition and exploitation of experimental data

To obtain data to fuel the model, we quantified three cell populations during cortical neurogenesis: APs, IPs, and Ns. For this quantification, we performed immunofluorescence on thin sections, with a combination of markers (S3 Table and S4 Table and Fig 3.2). We counted cell populations in a window of constant width ( $w$  in Fig 3.2B), which includes the whole thickness ( $th$  in Fig 3.2B) of the cortex, at all stages (Fig 3.2A-E). With this strategy, the increase in the AP number due to proliferative divisions, which occurs mainly before, but also at early stages of cortical neurogenesis, is not fully taken into account. Indeed, these proliferative AP divisions increase not only cell crowding in the pseudo-stratified VZ but also the surface of the VZ [29]. For this reason we decided not to use our AP quantifications in the model. This strategy also leads to an underestimation of the increase in neuronal numbers during cortical neurogenesis, since neurons, in addition to migrating radially into the cortical plate, display a certain level of tangential dispersion. Moreover, at late stages of cortical neurogenesis (from E17.5 onward), the density of neuronal nuclei decreases, most probably due to neurite outgrowth, which results in a decrease in the number of neurons in the quantification window. For this reason, we did not take into account neuron numbers at E17.5 and E18.5. In order to estimate the proportion of IPPs and IPNs, we quantified the number of  $Pax6^+Tbr2^+$  progenitors, proposed previously to represent the pool of IPPs [12, 34]. Fig 3.2F-H represents the experimental cell numbers in wild-type (blue) and  $Ftm^{-/-}$  (red) cortices at different developmental stages. The three panels correspond respectively to the IPs (F), IPPs (G) and neurons (H).



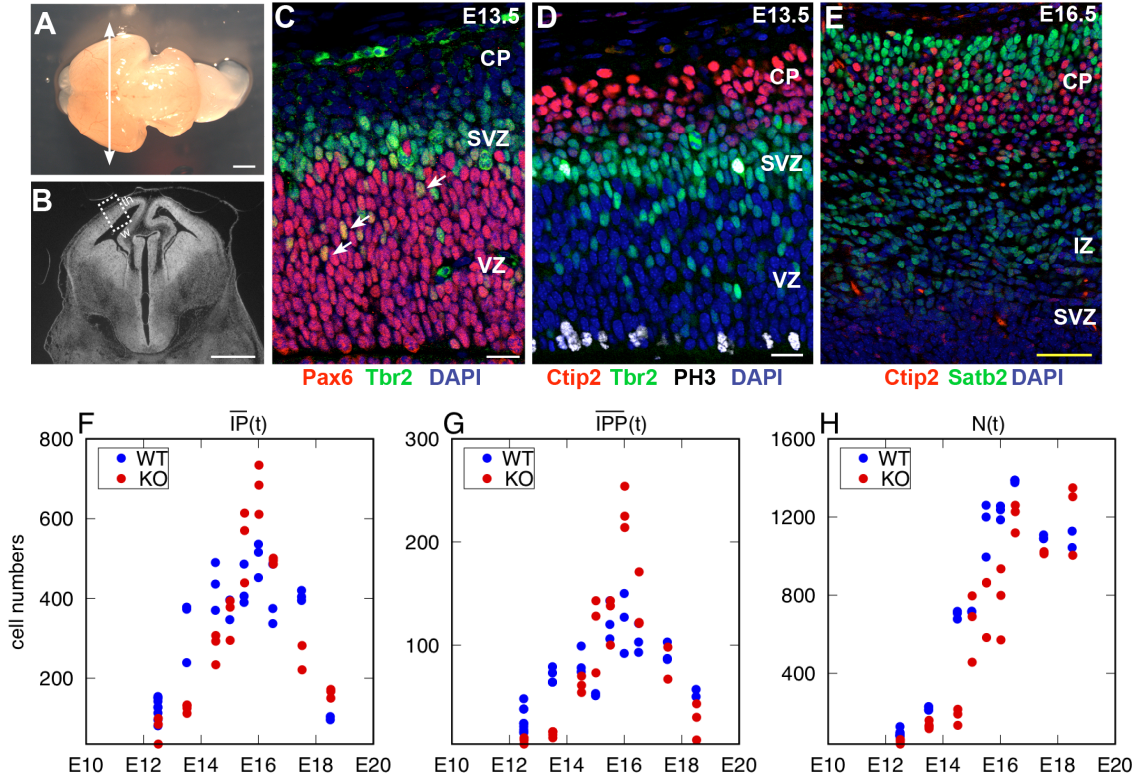


Figure 4: *Experimental cell counts: protocol and results* (A) Dorsal view of a wild-type E16.5 mouse brain. The level of the coronal sections used in this study is indicated by a white double arrow. (B) Coronal cryosection of an E13.5 mouse brain corresponding to the level of section shown in A. The window used for the quantification is framed.  $w$ : width;  $th$ : thickness. (C-E) Confocal scanning micrographs ( $1\mu\text{m}$  single optical section) of coronal sections of the dorsal telencephalon at E13.5 (C&D) and E16.5 (E). (C) Immunostaining with antibodies against Pax6 and Tbr2. DAPI counterstaining is used to label all the nuclei. White arrows show a selection of Pax6<sup>+</sup>Tbr2<sup>+</sup> nuclei (IPPs). (D) Immunostaining with antibodies against Tbr2, PH3 (to label cells in M-phase), Ctip2 (to label neurons). (E) Immunostaining with antibodies against Ctip2 (to label deep layer neurons) and Satb2 (to label upper layer neurons). IZ: Intermediate Zone. Scale bars: 1 mm in A, B,  $50\mu\text{m}$  in C, D,  $150\mu\text{m}$  in E. (F-H) Experimental cell counts for control (WT, blue dots) and *Ftm*<sup>-/-</sup> (KO, red dots) samples.

### 3.3 Model simulation and parameter calibration

To simulate the model equations, we first need to specify the values of the durations of the cell cycle phases. We also have to choose specific formulations for the rate functions  $\beta(t)$  (rate of IPgenic AP divisions) and  $\gamma(t)$  (rate of IPPgenic AP divisions over total IPgenic AP divisions) and the AP inflow rate  $F_{AP}(t)$ .

A natural choice is to use sigmoid functions for  $\beta(t)$  and  $\gamma(t)$ . Each function involves four parameters  $\beta_0$  (respectively  $\gamma_0$ ),  $\beta_1$  (resp.  $\gamma_1$ ) corresponding to their value at respectively  $-\infty$  and  $+\infty$ , and  $s_\beta$  (resp.  $s_\gamma$ ),  $t_\beta$  (resp.  $t_\gamma$ ) which control respectively the slope and location of the inflexion point.

$$\beta(t) = \beta_1 + \frac{\beta_0 - \beta_1}{1 + e^{s_\beta(t-t_\beta)}}, \quad \text{with } s_\beta > 0, \quad \gamma(t) = \gamma_1 + \frac{\gamma_0 - \gamma_1}{1 + e^{s_\gamma(t-t_\gamma)}}, \quad \text{with } s_\gamma > 0 \quad (10)$$

The formulation of  $F_{AP}(t)$  should take into account both the initial increase in the number of APs engaged in neurogenesis (hence the increase in IPgenic and possibly neurogenic divisions of APs at the

expense of proliferative divisions), and the exhaustion of the AP pool through the end of neurogenesis. Thus, we need to define a function whose shape would include both an ascending and descending part, possibly separated by a plateau. Note that, in contrast to  $\beta(t)$  and  $\gamma(t)$  which are dimensionless,  $F_{AP}(t)$  has the physical unit of a cell number. To preserve the possibility of subsequent interpretation in terms of division type and glial transformation, we combine a constant scale factor with two rate-like rise and decay functions (hence bounded between 0 and 1):

$$F_{AP}(t) = K_{AP} \frac{e^{s_+(t-t_+)}}{(1 + e^{s_+(t-t_+)}) (1 + e^{s_-(t-t_-)})} \quad (11)$$

$K_{AP}$  is the scale factor. Parameters  $t_+$  and  $t_-$  denote the time at the middle of the ascending and descending parts. Parameters  $s_+$  and  $s_-$  control the absolute value of the corresponding slopes. We thus ensure that for  $t \ll t_+ < t_-$  and  $t \gg t_- > t_+$ ,  $F_{AP}(t) \rightarrow 0$ . As a consequence, in the model the final neuron number is achieved when all other cell compartments have been emptied.

### 3.3.1 Control of the neuronal pool

Before proceeding to the model calibration, we illustrate here, in the simplified framework of constant rates, the effect of  $\beta$  (impacting the indirect neurogenesis) and  $\gamma$  (impacting the IPP production) on the size of the final neuronal pool as well as the transient changes in the neuron number. For each AP entering neurogenesis, we can compute the global neuronal yield from the relative proportions of each division type:

$$r_{AP}^N = (1 - \beta) + 2\beta(1 - \gamma) + 4\beta\gamma = 1 + \beta(1 + 2\gamma). \quad (12)$$

$r_{AP}^N$  would equal 1 if there was only direct neurogenesis from APs ( $\beta = 0$ ), 2 if there was no direct neurogenesis and no IP undergoing two division cycles ( $\beta = 1, \gamma = 0$ ), and 4 if there was no direct neurogenesis and all IPs underwent two division cycles ( $\beta = 1, \gamma = 1$ ). Beyond these schematic situations,  $r_{AP}^N$  can take any value between 1 and 4, and remains unchanged on isovalues of  $\beta(1 + 2\gamma)$  as shown in Fig 3.3.1.

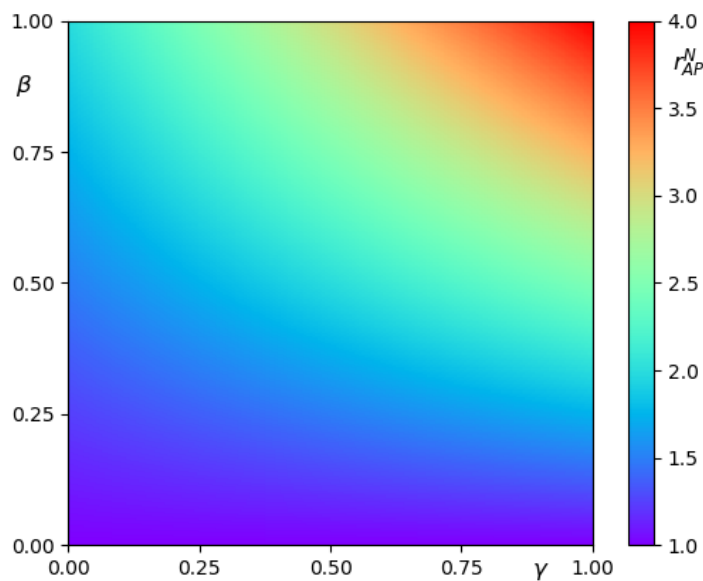


Figure 5: Ratio of total neuron production over total AP entering neurogenesis, as a function of  $\gamma$  and  $\beta$ , for constant coefficients. The color code for  $r_{AP}^N = 1 + \beta(1 + 2\gamma)$  is indicated on the right.

Fig 3.3.1 displays the changes in the numbers of IPs (Fig 6A), IPPs (Fig 6B) and neurons (Fig 6C), as a function of time, for different values of  $\gamma$  and in the absence of direct neurogenesis ( $\beta = 1$ ). As expected the maximum and cumulated numbers of IPPs and IPs increase with  $\gamma$ , and consequently the final number of neurons. Increasing  $\gamma$  also delays the onset of neuron production.

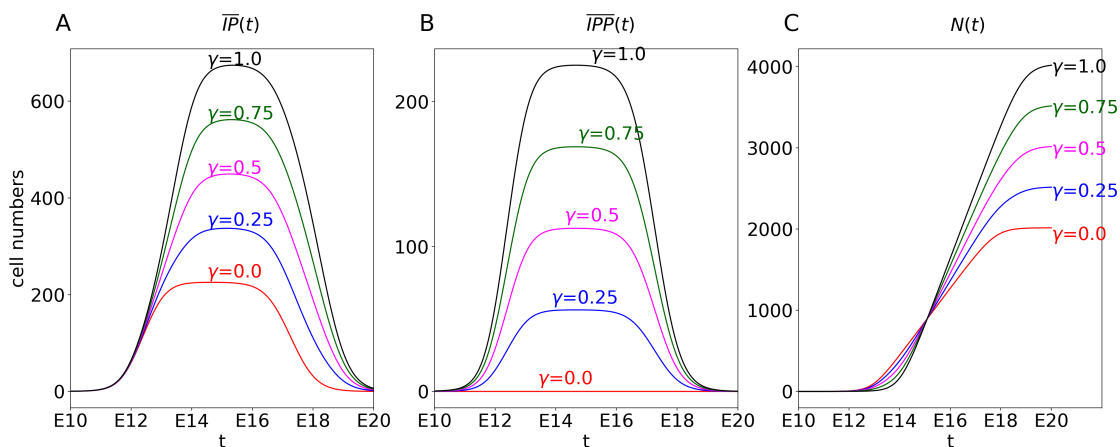


Figure 6: Influence of  $\gamma$  on  $\overline{IP}(t)$  (A),  $\overline{IPP}(t)$  (B) and  $N(t)$  (C). No direct neurogenesis and same cycle duration ( $T_C = 26.2$ ) for both type of IPs, parameters for  $F_{AP}(t)$  as in line #3 of Table 3.3.2.

In Fig 3.3.1, we now keep  $\gamma$  constant, as well as  $\beta = 1$ , and let the IPP cell cycle duration vary from 21 to 37 hours (the reference duration being 29.4 hours). A high value has been chosen for  $\gamma$  (0.9) in order to get a pronounced effect of the IPP cell cycle duration on the outputs. Shortening the cycle advances the production of neurons, since IPPs exit the cell cycle and divide into IPNs earlier.

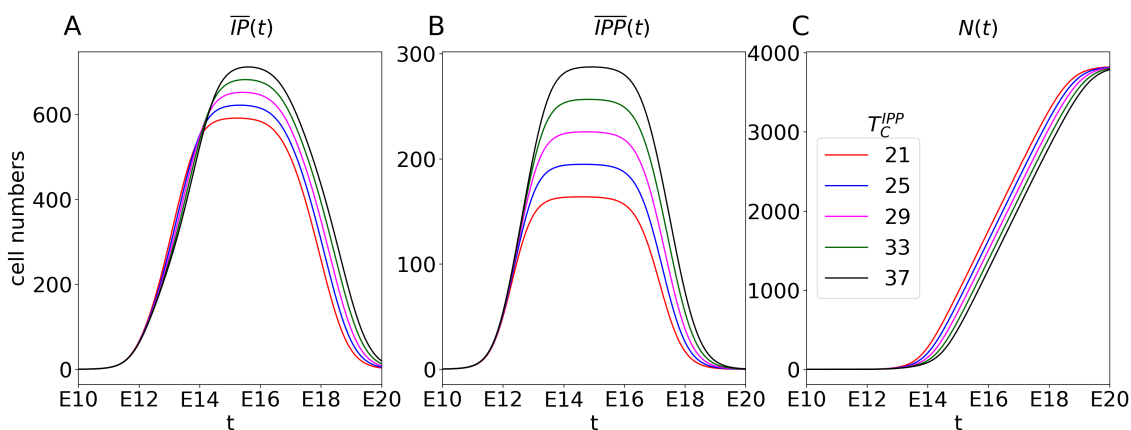


Figure 7: Influence of  $T_C^{IPP}$  on  $\overline{IP}(t)$  (A),  $\overline{IPP}(t)$  (B) and  $N(t)$  (C). No direct neurogenesis and constant  $\gamma(t) = 0.9$ . Parameters for  $F_{AP}(t)$  as in line #3 of Table 3.3.2.

These simulations illustrate how the proportion of IPPs tunes the amplifying factor of neuron generation, as defined by (12). In contrast, the duration of the IPP cell cycle impacts the kinetics of neuron formation without affecting the final neuron number.

### 3.3.2 Parameter calibration on experimental data

A priori information can be used for some of the model parameters, such as the durations of the cell cycle phases provided in Arai et al. [1] (see S2 Table), a study which provides a comprehensive description of the cell cycle in each progenitor type depending on the fate of its progeny. In order to distinguish IPPs and IPNs, Arai et al. [1] made use of the Tis21-GFP transgenic mouse line, in which GFP is selectively expressed in neuron- generating progenitors [16].

Our experimental data consist in cell counts of intermediate progenitors and neurons, on a daily basis between E12 and E18. Double stained  $Pax6^+Tbr2^+$  cells can be considered as a rough estimate of IPPs.

We designed a fit function to measure the adequation between our model and the experimental cell numbers

$$\begin{aligned}
 J(p) = & C_N \sum_t |N(t, p) - N^{exp}(t)|^2 + C_{IP} \sum_t |\overline{IP}(t, p) - IP^{exp}(t)|^2 \\
 & + C_{IPP} \sum_t |\overline{IPP}(t, p) - IPP^{exp}(t)|^2
 \end{aligned} \tag{13}$$

where  $N^{exp}(t)$ ,  $IP^{exp}(t)$  and  $IPP^{exp}(t)$  are the experimental values at a given time, averaged over the replicates (see S4 Table). The number of replicates (i.e. of individual measures in a same group -WT or KO- at the same time) is too low to obtain reliable time-dependent weights. We rather use global multiplicative weights  $C_N$ ,  $C_{IP}$  and  $C_{IPP}$  to counterbalance the differences in the amplitude of cell numbers from one cell type to another, in order to give a similar importance to each of them.

We minimize  $J(p)$  over the set

$$\mathcal{P} = \{p = (K_{AP}, s_+, t_+, s_-, t_-, \beta_0, \gamma_0, \gamma_1, s_\gamma, t_\gamma), p_i \in [p_{\min}^i, p_{\max}^i], i = 1, \dots, 10\}. \tag{14}$$

The parameter space is a subset of  $\mathbb{R}^{10}$  and the parameter bounds are either imposed, for instance  $(\beta_0 = \beta_1, \gamma_0, \gamma_1) \in [0, 1]^3$  or chosen sufficiently large to be inactive at the minimum. On the other hand, the experimental data are time sampled on a coarse, daily basis in the limited E12-E18 time window, and the inter-replicate dispersion can be quite large, as displayed in Fig 3.2. As a consequence, the  $J(p)$  functional exhibits several local minima, so that it can hardly be minimized with a descent method. It is why we chose to apply the CMAES stochastic method [15] to overcome the problem of the initial parameter guess, which is crucial in deterministic identification methods.

We performed several simulations with different sets of parameters obtained from the minimization of  $J(p)$ . For each simulation, we compute, in addition to the model outputs:

- the fit value  $J(p^*)$  for  $C_{IP} = 5$ ,  $C_N = 1$  and  $C_{IPP} = 0$ ,
- the fit value  $J(p^*)$  for  $C_{IP} = 5$ ,  $C_N = 1$  and  $C_{IPP} = 5$ ,

where the value of  $C_{IP}$  is chosen so as to compensate for the 5-fold difference in amplitude between the numbers of neurons and IPs or IPPs,

- the ratio between the number of produced neurons and the number of APs which have entered neurogenesis in the course of the simulation, from initial time  $t = 0$  to stopping time  $t = T$ , which we set equal to E20 in the numerical simulations

$$r_{AP}^N(T) = \frac{N(T)}{\int_0^T F_{AP}(t) dt}, \tag{15}$$

which can also be directly estimated from the extension of formula (12) with time-dependent rates:

$$r_{AP}^N(T) = \frac{1}{T} \int_0^T 1 + \beta(t) + 2\beta(t)\gamma(t) dt.$$

The values of criterion (13) and parameter sets are gathered in Tab. 3.3.2. We first adjusted the model parameters from the neuron and total IP numbers of the WT dataset, with  $C_N = 1$ ;  $C_{IP} = 5$ , and  $C_{IPP} = 0$  with either a constant (scenario 1,  $\gamma = 1$  green line in Fig 3.3.2) or time-varying  $\gamma(t)$  (scenario 2, blue line), and then we also included the IPP cell number in the dataset ( $C_{IPP} = 5$ , scenario 3, red line). In all three cases, parameter  $\beta$  is estimated as a constant, since we did not observe any time variation in this parameter in a series of preliminary optimization studies.

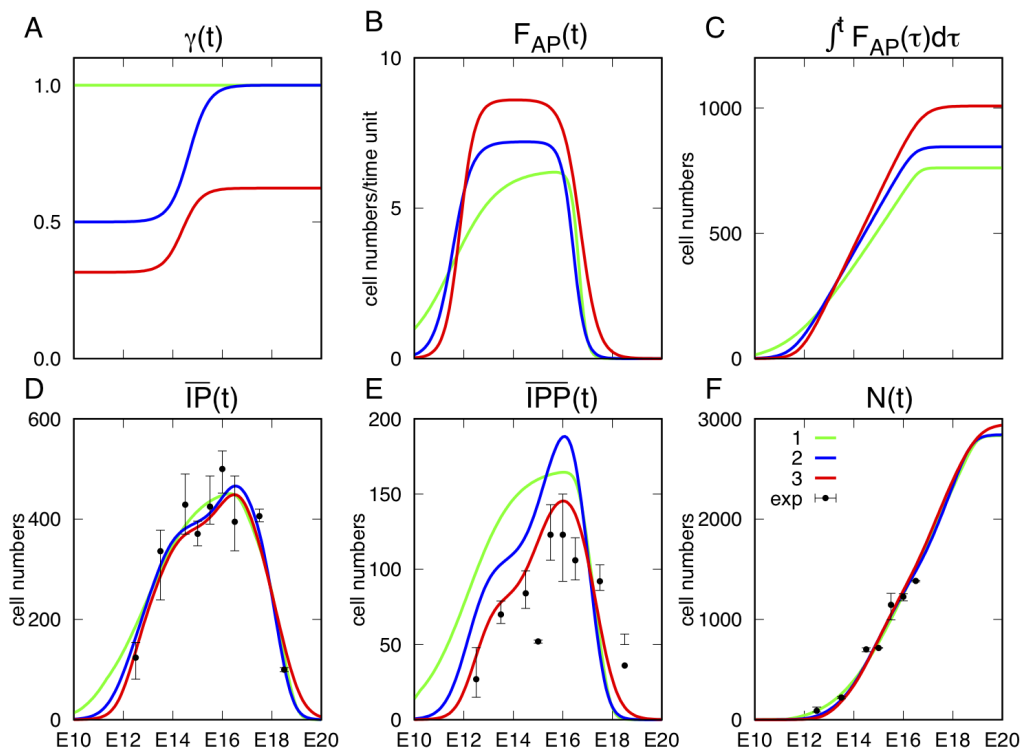


Figure 8: Optimization results on the control dataset. Coefficients and outputs of the model for the three parameter sets in Table 3.3.2, superimposed on experimental values represented by their mean and global range (in black). Green (#1) and blue (#2) lines correspond to a fit with neurons and IPs, red lines (#3) correspond to the fit including IPPs. Green lines correspond to the fit with  $\gamma(t)$  kept constant. Panel (A) displays the division rate  $\gamma(t)$ . Panel (B) displays the input flux of AP cells  $F_{AP}(t)$ . Panel (C) displays the cumulative number of AP cells  $\int_0^t F_{AP}(\tau) d\tau$ . Panel (D) displays  $\overline{IP}(t)$  computed by the model (5). Panel (E) displays  $\overline{IPP}(t)$  computed by the model (4). Panel (F) displays  $N(t)$  computed by the model (6). The value of the ratio  $r_{AP}^N$  for the three simulations is 3.72 (scenario 1 in green), 3.37 (scenario 2 in blue) and 2.93 (scenario 3 in red).

All three scenarios lead to rather similar pattern for the neuron curve. In scenario 1, the absence of direct production of IPNs from APs ( $\gamma = 1$ ), which could be expected to lead to delayed N production, is actually compensated for by the direct production of Ns from APs.

In contrast, these scenarios clearly differ as far as fitting IP numbers. Scenario 1 fails to capture correctly the initial rise in IPs, which occurs too early with respect to the experimental data. Accordingly, the criterion  $J(p)$  is better optimized in scenario 2. In addition, the improvement remains similar if  $J(p)$  is computed again by adding a posteriori (i.e. keeping the same parameter set without performing a new optimization run) the contribution of IPP data, so that there is real gain in selecting a time-dependent

formulation of parameter  $\gamma(t)$ .

Scenario 3 is rather close to scenario 2 for Ns (even if the neuronal yield  $r_{AP}^N$  is slightly lowered) and total IPs. Yet, as expected, the fitting to IPP data is drastically improved and involves a downward translation of the  $\gamma(t)$  curve. There remains a shift to the right along the descending part of the IPP curve, which can be explained by the discrepancy observed between the experimental IP and IPP datasets (WT IPP values exceed IP values at E18.5, see panels F and G of Fig 3.2) at the end of neurogenesis. As discussed elsewhere, IPP are identified as  $Pax6^+Tbr2^+$  cells; this marker appears to be less reliable during late neurogenesis.

#		1(WT)	2(WT)	3(WT)	4(KO)	5(KO)
$T_C^{IPP}$		29.4	29.4	29.4	29.4	35.4
$J(p)$	$C_{IPP} = 0$	158	125	171	180	188
	$C_{IPP} = 5$	332	265	212	256	232
$r_{AP}^N$		3.72	3.37	2.93	2.70	2.58
$F_{AP}$	$K_{AP}$	6.29	7.22	8.62	40	40
	$s_+$	1.09	2.62	3.34	1.27	0.91
	$t_+$	11.55	11.55	11.84	14.54	15.45
	$s_-$	6.3	4.16	2.80	1.44	5.91
	$t_-$	16.65	16.42	16.71	15.12	16.01
$\beta$		0.91	1	1	1	1
$\gamma$	$\gamma_0$	1	0.5	0.31	0	0.26
	$\gamma_1$	NA	1.00	0.62	0.45	1.00
	$s_\gamma$	NA	2.53	2.65	10.00	10.00
	$t_\gamma$	NA	14.65	14.38	13.73	16.17

Table 1: Different cases for parameter estimation. The five simulations, illustrated in Fig 3.3.2 and 3.3.2, are performed with parameters fitted on wild type (WT) or *Ftm* mutant (KO) data, taking a cell cycle duration of 29.4h for the IPP cell type as in [1], except in case 5 (35.4h). The  $\gamma(t)$  rate is either a constant (cte) or a sigmoid function of time (var), and the datasets used in the fit (13) include IPs and Ns in all cases, and additional data on IPPs in cases 3 to 5. The parameter values obtained from optimization are highlighted in blue. The corresponding a priori criterion values are highlighted in red. The values of the criterion recomputed a posteriori with adding (upper line) or removing (lower line) the IPP dataset are left in black.

The simulations displayed in Fig 3.3.2 can be reproduced with an Ipython notebook, CEMONE<sup>1</sup> which can be either downloaded from <https://github.com/letsop/cehone> or directly run on <https://mybinder.org/v2/gh/letsop/cehone/master>

From the results obtained on the control dataset, we directly performed the parameter optimization on the mutant dataset in a situation similar to scenario 3 (time-dependent  $\gamma(t)$  and  $C_{IPP} = 5$ , scenario 4 in Table 3.3.2). We compare the control and mutant results in Fig 3.3.2. The differences observed in the experimental datasets mainly concern the IP (and IPP) peak, which is higher and narrower, and also occurs later in mutant mice compared to control. This difference can be explained by the observed alteration in the patterns of  $\gamma(t)$  and  $F_{AP}(t)$ . In the mutant case,  $\gamma(t)$  is not only shifted downwards, to the point that the minimal value sticks to the zero floor at the beginning of neurogenesis, but also its shape is distorted, with a much sharper increase from 0 to 0.45 just before E14 (panel A). In the meantime  $\gamma(t)$  rises from 0.37 to 0.62 in the control case.  $F_{AP}(t)$  also changes in a very different manner (panel B). Rather than reaching a plateau, hence being almost constant during most of the neurogenesis period (from E14 to E16), the flux of committed APs in the mutant case is both peak-shaped and condensed in time. In the control case, the increase in the cumulated flux is close to linear and reaches a steady value around E17. In the mutant case, the curve is first sublinear and then becomes superlinear, so that it crosses the control curve before reaching a steady value. Nevertheless, the total number of APs entering

<sup>1</sup>CELL based MOdel of NEurogenesis

neurogenesis (panel F) is very similar, and the neuronal yield is almost as high in mutant (2.70) as in control (2.93).

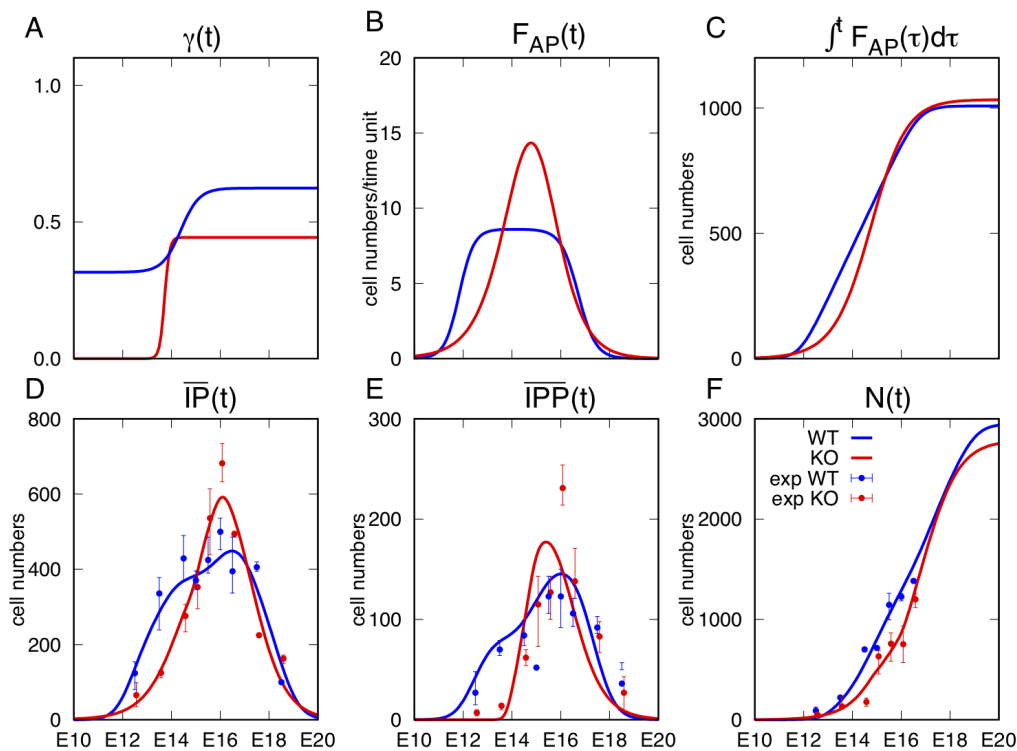


Figure 9: Comparison of wild-type (WT, in blue) and  $Ftm^{-/-}$  (KO, in red) results. Coefficients and outputs of the model for the parameter sets #3 and #4 in Table 3.3.2, superimposed on experimental values represented by their mean and global range. Panel (A) displays IPPgenic division rate of APs,  $\gamma(t)$ . Panel (B) displays the input flux of AP cells,  $F_{AP}(t)$ . Panel (C) displays the cumulative number of AP cells entering neurogenesis,  $\int_0^t F_{AP}(\tau) d\tau$ . Panel (D) displays  $\bar{IP}(t)$  computed by the model (5). Panel (E) displays the IPP number curve  $\bar{IPP}(t)$  computed by the model (4). Panel (F) displays the neuron number curve  $N(t)$  computed by the model (6). The blue (respectively red) dots and vertical bars correspond to the mean values and whole range of the control (resp. mutant) experimental dataset. The ratio  $r_{AP}^N = 2.93$  for the control and  $r_{AP}^N = 2.70$  for the mutant.

Note that the changes in the cumulated AP flux and neurons look similar in controls and mutants, yet they are not identical. In the model, the IP dynamics operate as a transfer function from the AP input to the N output. As observed in the case of constant rates, the proportion of IPPs tunes the amplification factor of neuron production, while the durations of the IPP and IPN cell cycles impact the kinetics of neuron apparition and further increase.

In the previous comparison, we have used the same durations of cell cycles for the mutant and control cases. Yet, we cannot exclude that the cell cycle durations may differ between controls and mutants. We have thus explored the effect of varying systematically the IPP cell cycle duration (which affects the cell dynamics in a more complicated way than the IPN one). For each tested duration, from 26.4 to 35.4h, we have performed again the estimation procedure. Whatever the duration, the direct neurogenesis rate from APs happened to be null ( $\beta = 1$ ). The best fit over all durations only resulted in a 10% improvement of the optimization criterion (scenario 5 in Table 3.3.2). Since the fitting improvement was modest and

the corresponding 35.4h duration rather high, we retained scenario 4 for the sake of modeling parcimony.

In both the control and mutant cases, we had to optimize a fitting criterion with a relatively large number of parameters, some of them entering in addition the time-varying rate functions  $F_{AP}(t)$ ,  $\beta(t)$  and  $\gamma(t)$ . There is a limit to the number of independent parameters that can be identified using a given dataset, which depends on the number and repartition of the measurements within the time window. Note that if in a linear model adjustment this dependence is straightforward, in the case of a non linear model such as ours, it is not easy to establish. Furthermore, theoretical identifiability does not ensure that a practical solution can be easily obtained. Even if the minimization problem (13,14) has a global solution, it might be hidden among several local minima and very hard to compute. Nevertheless, our optimization procedure has benefited a lot from being fueled with a combination of data, involving not only IP cell numbers, but also neuron numbers. Further improvement of the parameter estimation could be obtained with more accurate information on the size of final neuron pool and on the distinction between IPP and IPN cells (for instance using the Tis21-GFP transgenic line).

In the case of the *Ftm* mutant, our simulations suggest that the perturbed dynamics of neurogenesis cannot be accounted for by a clear difference in IP proliferation mode or division rate. The model allows us to predict that obtaining a similar neuronal output with a shorter neurogenesis period requires an important and transient inflow of APs ( $F_{AP}$ ).

### 3.4 Derivation of cell kinetics indexes and associated quantitative information on proliferative versus neurogenic cell populations

In our experimental setup, we have considered, following [12] and [7], that the specific combination of Pax6 and Tbr2 staining can help discriminate IPPs from IPNs. Other experimental markers derived from cell kinetics principles have been proposed in the literature [33]. The mitotic index (MI; ratio of cells in M phase) and the labeling index (LI; ratio of cells in S phase) in a given progenitor population can be assessed with experimental labeling. This can be achieved for instance using immunoreactivity for phosphorylated Histone H3 (to label M phase), and incorporation into the DNA of nucleoside analogs such as BrdU, EdU or IddU followed by their immunofluorescence detection (to label S phase). We now explain how to compute such indexes *in silico* and to use the model outputs to assess their robustness to either extrinsic (such as the time chosen to perform the measurements) or intrinsic (such as the duration of cell cycle and cell cycle phases) factors.

**Ratios based on the mitotic index** Several studies have intended to quantify neurogenic mitoses in AP and IP populations, using different approaches [1, 12, 17]. Here we show that we can use the model to assess the ratio of IPs and APs committed to a neurogenic division.

The ratio  $\psi(t)$  of neurogenic IP mitoses can be computed exactly from the direct counting of mitotic cells (cf Eq. 7) as

$$\psi(t) = \frac{\overline{IPN}_M(t)}{\overline{IPP}_M(t) + \overline{IPN}_M(t)}. \quad (16)$$

Since phase M is relatively short compared to the cell cycle duration, we can also estimate  $\psi(t)$  from the fluxes of cells getting out of either the IPP or IPN cell cycles

$$\psi(t) \approx \frac{IPN(t, T^{IPN})}{IPN(t, T^{IPN}) + IPP(t, T^{IPP})} \quad (17)$$

These quantities can be computed using the method of characteristics

$$\psi(t) \approx \frac{IPN(t - T^{IPN}, 0)}{IPN(t - T^{IPN}, 0) + IPP(t - T^{IPP}, 0)}.$$



The incoming cell flux into the IPN cell cycle is composed of the contribution of both APs and IPgenic IPPs

$$\begin{aligned} IPN(t,0) &= F_{AP}(t)(1 - \gamma(t))\beta(t) + 2IPP(t, T^{IPP}) \\ &= F_{AP}(t)(1 - \gamma(t))\beta(t) + 2IPP(t - T^{IPP}, 0) \end{aligned} \quad (18)$$

while only AP divisions contribute to the incoming cell flux into the IPP cell cycle

$$IPP(t,0) = F_{AP}(t)\gamma(t)\beta(t). \quad (19)$$

Even if we do not represent as such the dynamics of APs, the model also allows us to compute the number of neurogenic AP mitoses from the cell fluxes getting out of the AP compartment (following the same approximation based on the short duration of phase M as above).

As shown in panel C of Figs. 3.4 and 3.4, the agreement between the approximation obtained by plugging (18) and (19) into (17) and the exact computation (16) is very good as soon as the number of mitotic cells is large enough, which guarantees that the denominator of (16) is not too close to zero (which can happen when the cycles get emptied from their cells). Fig 3.4 illustrates the changes in the neurogenic fraction of mitoses (panel C) as well as in the MI (panel B) and LI (panel A), in a simplified parameter framework (constant  $\gamma$ ,  $\beta = 1$ ,  $T_S^{IPP} = T_S^{IPN}$ , combined with the  $F_{AP}(t)$  flux function of scenario 3 of Table 3.3.2).

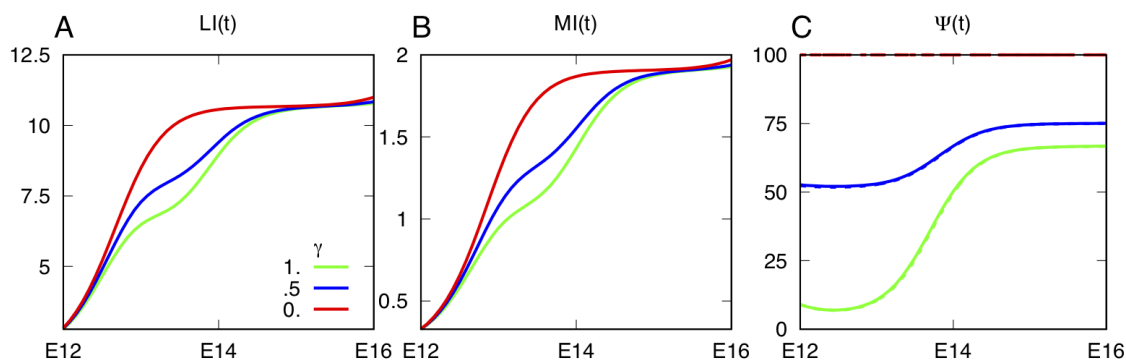


Figure 10: Cell kinetics indexes for a simplified parameter set ( $F_{AP}$ , from scenario 3 of Table 3.3.2,  $\beta = 1$ , and identical cell cycle phases for both IPPs and IPNs, second line in S2 Table). We keep  $\gamma(t) = cte$  with three possible values 0 (in red), 0.5 (in blue) and 1 (in green). Panel A displays the labeling index (LI, in percent) for total IPs (8). Panel B displays the mitotic index (MI, in percent) for total IPs (9). Panel C displays the ratio of neurogenic IP mitoses (in percent),  $\psi(t)$ , computed with (16) (solid lines), along with the estimate (17) (dashed lines).

Fig 3.4 shows the same panels for each of the scenarios 1 to 4 of Table 2. In particular, the neurogenic fraction obtained with scenario 3 constitutes a prediction of the model. Interestingly, this prediction is consistent with the results obtained in [17]. In this work, the authors have taken advantage of the Tis21-GFP staining in combination with Pax6 or Tbr2, in addition to PH3, to identify the neurogenic fate of APs and IPs in a specific way. They have shown that a significant proportion of IP mitoses are not neurogenic and that very few AP mitoses are neurogenic, which corroborates the very low, or even neglectible value of direct neurogenesis from AP in our setup.

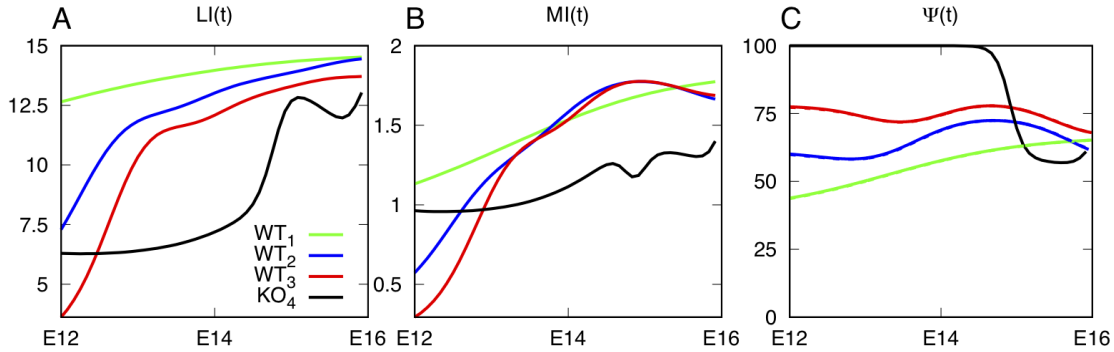


Figure 11: Cell kinetics indexes for parameters of scenarios 1 to 4 of Table 3.3.2. Same legend as Fig 3.4.

**Ratios based on the labeling index** *Experimental rationale.* Cumulative labeling [1] or double labeling [23] by incorporation of nucleoside analogs is classically used to assess the duration of S phase. Another application of S phase double labeling was proposed to try to discriminate, within a given progenitor cell population, cells undergoing a second round of division from cells progressing along their first cell cycle within this cell type [33]. In this case, the delay between the administration of both dyes is much longer, on the order of the duration of a cell cycle (and should be finely tuned as explained below), and cells are labeled sequentially from one generation to the next (only daughter cells can be double-labeled). In more details, the experimental protocol consists in administering first BrdU at a given time  $t_1$ , and then, after an appropriate (and long) delay  $t_2 - t_1$ , EdU. After  $t_2$ , the number of double-labeled ( $BrdU^+EdU^+$ ) cells is an estimate of the number of cells that have gone through two rounds of S phases since  $t_1$ , while single-labeled ( $BrdU^-EdU^+$ ) cells were not in S phase at the time of BrdU injection.

*In silico assessment.* Here we focus on the *in silico* assessment of double-labeled cells in the case of the IP population, and highlight its sensitivity to extrinsic (choice of the delay between BrdU and EdU administration) and intrinsic (differences in S phase duration between IPP and IPN) factors.

As in the case of the ratios derived from mitotic indexes, one great advantage of the modeling approach is to have access to the reference (“true”, computed) value, and to be able to compare the estimated values with respect to this reference.

The number of IPPs in S phase, hence labeled with BrdU, at  $t_1$  is given by:

$$\overline{IPP}_S(t_1) = \int_{T_{G1}^{IPP}}^{T_{G1}^{IPP} + T_S^{IPP}} IPP(t_1, a) da. \quad (20)$$

Hence, the reference value is  $2 \overline{IPP}_S(t_1)$  (factor 2 accounts for the occurrence of mitosis in  $BrdU^+$  cells during the  $t_2 - t_1$  interval). Note again that this number is not available as such in the experimental protocol, and is rather approximated from the number of  $BrdU^+EdU^+$  cells.

On the other hand, at  $t_2$ , the total number of IPs labeled with EdU corresponds to the number of IPs progressing along S phase. Amongst these, only IPNs may have undergone a former cell cycle as IPPs and are susceptible to be double labeled. We derive in the Material & Method section, the cell number  $\overline{IPN}_S^*(t_2)$  (eq 25) mimicking the experimental values of double  $BrdU^+EdU^+$  labeled cells as a function of the  $t_2 - t_1$  delay and durations of cell cycle phases.

The computation of  $\overline{IPN}_S^*(t_2)$  amounts to removing all possibly “false positive” double labeled cells, which is a modeling issue (since we cannot stain cells in the model). In the next session, we will also deal with “false negative” cells, which is really an experimental issue, that may lead to underestimate the number of IPPs in S phase at  $t_1$ .

*Optimal protocol design : sensitivity to the delay and S phase durations.* Now, we can compare

the experimental-like estimated value,  $\overline{IPN}_S^*(t_2)$ , with the reference value,  $2\overline{IPP}_S(t_1)$ , according to the chosen  $t_2 - t_1$  delay and the difference in S phase durations between IPPs and IPNs. In consistency with biological knowledge, we restrict our study to the case when  $T_S^{IPP} \geq T_S^{IPN}$ , yet it can be easily generalized to the opposite case. The quality of the estimation can be summarized by the proportion of detected cells (positive predictive value)  $\rho$ :

$$\rho = \frac{\overline{IPN}_S^*(t_2)}{2\overline{IPP}_S(t_1)}. \quad (21)$$

1. If  $t_2 - t_1 \leq T_{G2}^{IPP} + T_M^{IPP} + T_{G1}^{IPN}$ , then no BrdU+ cells has had the time to reach S phase by  $t_2$ , and  $\rho = 0\%$ ;
2. If  $T_{G2}^{IPP} + T_M^{IPP} + T_{G1}^{IPN} < t_2 - t_1 < T_{G2}^{IPP} + T_M^{IPP} + T_{G1}^{IPN} + T_S^{IPN}$  then a subpart of Brdu+ cells lie within a new S phase and will be detected as BrdU+EdU+ cells. The value of  $\rho$  increases as linearly  $t_2 - t_1$  increases;
3. If  $T_{G2}^{IPP} + T_M^{IPP} + T_{G1}^{IPN} + T_S^{IPN} < t_2 - t_1 < T_{G2}^{IPP} + T_M^{IPP} + T_{G1}^{IPN} + T_S^{IPP}$ , the value of  $\rho$  has reached a plateau, whose height increases as the ratio  $T_S^{IPN}/T_S^{IPP}$  increases, up to the maximal value of  $\rho = 100\%$  when  $T_S^{IPP} = T_S^{IPN}$ ;
4. If  $T_{G2}^{IPP} + T_M^{IPP} + T_{G1}^{IPN} + T_S^{IPP} < t_2 - t_1 < T_{G2}^{IPP} + T_M^{IPP} + T_{G1}^{IPN} + T_S^{IPP} + T_S^{IPN}$  then the value of  $\rho$  decreases linearly as  $t_2 - t_1$  increases;
5. If  $t_2 - t_1 \geq T_{G2}^{IPP} + T_M^{IPP} + T_{G1}^{IPN} + T_S^{IPP} + T_S^{IPN}$ , then all BrdU+ cells have overcome S phase by  $t_2$ , and  $\rho = 0\%$ .

In Fig 3.4, we illustrate the comparison between the true value ( $2\overline{IPP}_S(t_1)$ ) and the estimated one ( $\overline{IPN}_S^*(t_2)$ ), in the case of an optimal choice of the delay  $t_2 - t_1$  (case 3 above). In panel A, the duration of S phase is the same for IPPs and IPNs, and, as expected,  $\rho = 1$  (notwithstanding some discards due to numerical approximations). In panel B, the duration of phase S of IPP exceeds that of IPN, and consequently  $\rho$  is lower than 1. In Fig 3.4 we show the changes occurring in  $\rho$  according to the delay  $t_2 - t_1$  in the whole range covering cases 1 to case 5 above.

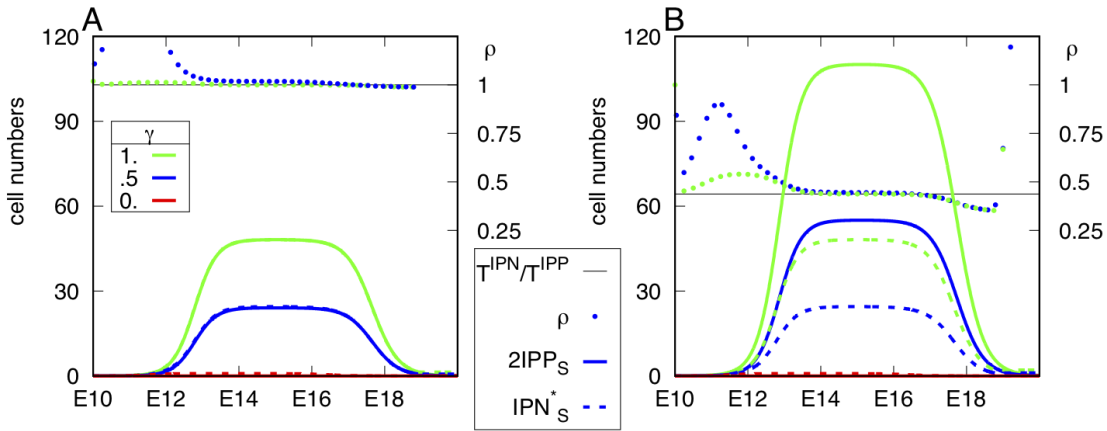


Figure 12: Comparison of the numbers of IPPs in S phase at  $t_1$  ( $2\overline{IPP}_S(t_1)$ ) (20), solid line) with their estimation from double BrdU+EdU+ labeled cells at  $t_2$  ( $\overline{IPN}_S^*(t_2)$ ) (25), dash lines). We use the same durations as those of S2 Table for the phases of the IPN cell cycle and all phases except S phase of the IPP cell cycle. In panel A,  $T_S^{IPP} = T_S^{IPN} = 2.8h$ , while, in panel B,  $T_S^{IPP} = 6.4h$  and  $T_S^{IPN} = 2.8h$ . The input flux  $F_{AP}(t)$  is the same as Case (3) of Table 3.3.2.  $\gamma(t) = cte$  (0, 0.5 or 1). The ratio  $\rho(t)$  between the estimated and the true value (eq. (21)) is also plotted on each panel, according to the scale ticked on the right axis, alongside the theoretical value  $T_S^{IPN}/T_S^{IPP}$  (in black).

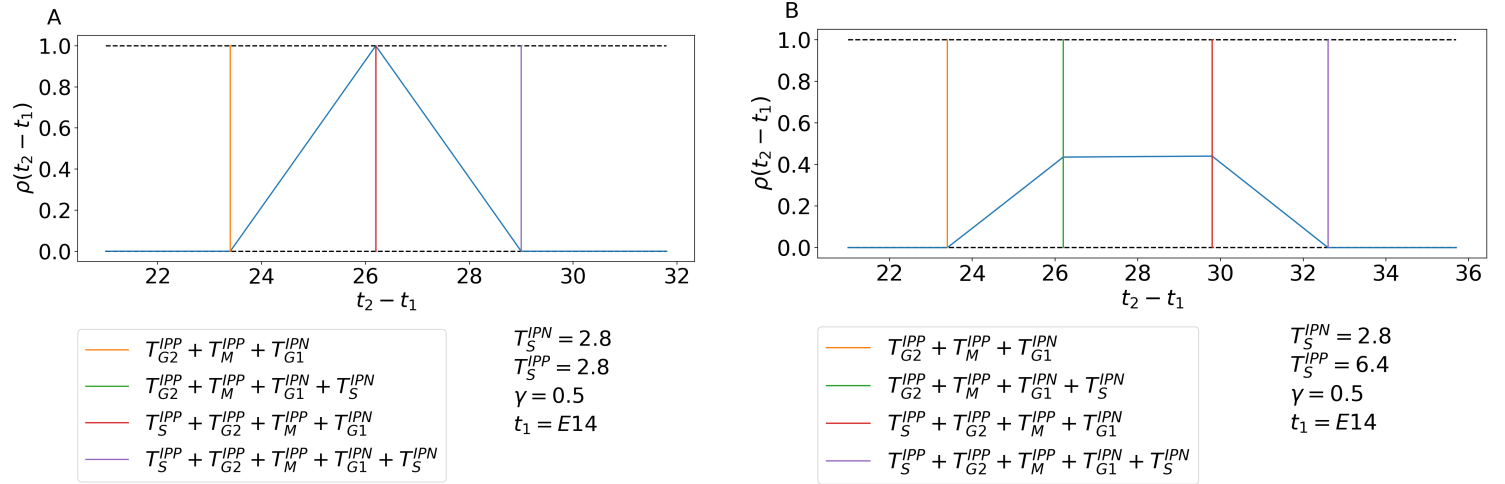


Figure 13: Sensitivity of the protocol to the delay and S phase duration. The two panels display the ratio  $\rho(t_2 - t_1)$  (eq. 21) as a function of  $t_2 - t_1$  for  $t_1 = E14$ . In each panel, the duration of the cell cycle phases are the same as the corresponding panels in Fig 3.4  $\gamma(t) = 0.5 = cte$ .

The computations have been done in the case of a pulse-mode labeling (instantaneous action). Actually, there is some remanence in the labeling, which could be accounted for by computing the index on a cumulated time interval adjusted to the dye duration effect. Yet, in practice, this amounts to lengthening the apparent duration of the corresponding S phases, and the reasoning remains exactly the same. A practical fallout of this remark is that, in the case when  $T_S^{IPP} \geq T_S^{IPN}$ , we can recommend to extend the administration of EdU with respect to that of BrdU.

In conclusion, our model allows us to compute cell kinetics indexes, associated with given IP and neuron temporal patterns such as shown in Fig 3.3.2 and 3.3.2. The dynamics of these indexes are complicated and non intuitive. In particular, the ordering of indexes in control and mutant reverses in time, so that we recommend to perform several time point measurements. If accurate and time detailed measurements of mitotic and labeling indexes were available, information on the cell cycle phase durations could be obtained by comparison with the model outputs (7-9). We have also illustrated the potential of the model to mimic and/or plan elaborate cell kinetics experiments based on the MI and LI indexes.

## 4 Material and methods

### 4.1 Mice, embryo collection and staging

All experimental procedures involving mice were performed in accordance with ethical guidelines of the European directive 2010/63/UE and its French application decree 2013-118, and were approved by the ‘‘Charles Darwin’’ local ethical committee with Project number 1382. The animal facility has obtained authorization from the Paris police Headquarters, DDPP (Direction D epartementale de la Protection des Populations) service, with authorization number B 75-05-24. Adult mice were euthanized by cervical dislocation or CO2 exposure. Fetuses before E16.5 were euthanized by decapitation. Fetuses after E16.5 were anesthetized by hypothermia before transcatheter perfusion (which led to death of the fetus). The *Ftm* mutant mouse line [6,32] was maintained at the heterozygous state in the C57Bl/6j background. Heterozygous mice were incrossed in order to obtain embryos and fetuses of the desired genotypes: *Ftm*<sup>+/+</sup> (wild-type, wt), *Ftm*<sup>+/-</sup> (heterozygotes) and *Ftm*<sup>-/-</sup> (homozygote mutant). *Ftm*<sup>+/+</sup> and *Ftm*<sup>+/-</sup> animals were viable and fertile and their phenotype was normal [6,32], hence they were collectively designated

as controls (ctrl or WT in figures and tables). Embryonic day (E) E0.5 was defined as noon on the day of vaginal plug detection. Stage variability between litters of the same theoretical chronological age may arise as a function of the time of mating and of the potential delay in fertilization. Dissections were always performed between 3 pm and 4 pm to minimize developmental variability across litters. In order to reduce further this variability, we obtained morphometric measurements on brain sections and used anatomical criteria (suppl. Material, S1 Fig). The histological criteria were i) the dorso-ventral extent of the 3rd ventricle (which, from E14.5 onward, progressively reduces by fusion of the left and right thalami, leaving only dorsal and ventral openings), ii) the presence of the choroid plexus in the dorsal part of the 3rd ventricle (from E14.5), iii) the thickness of the ventricular-subventricular zone in the dienecephalon (thick at E15.5, reduces afterward), iv) the folding of the hippocampus (starts at E15.5 and increases progressively) and v) the size of the caudal eminence (maximum at E16.5 and then decreases). Three adjacent brain sections were scanned using a Leica (DFC345FX) binocular. The stages of the litters were adjusted relative to each other, with a minimal 12 hour-delay between two consecutive time points.

## 4.2 Immunofluorescence

Brains of embryos younger than E16.5 were dissected in cold phosphate-buffered saline (PBS) and fixed overnight at 4°C in a solution of 4% paraformaldehyde in PBS (4% PFA). Fetuses at E17.5 and E18.5 were subjected to intracardial perfusion with 4% PFA under mild agitation; then their brains were dissected and kept in 4% PFA overnight at 4°C. The brains were then rinsed and mounted in Optimum Cutting Temperature (OCT) and cut on a cryostat into 14  $\mu\text{m}$ -thick serial sections. Prior to immunofluorescence, slides were boiled with 0.1M sodium citrate buffer in a microwave oven for antigen retrieval, washed in PBS and blocked for 1h in PBS containing 0.3% Triton X-100 and 10% goat serum. Sections were immunostained by overnight incubation with primary antibodies at 4°C. The following primary antibodies were used: Pax6 (Covance/eurogentec PRB-278P; 1:500), Tbr2 (Abcam 23345; 1:300) Tbr2-alexa488 (Ebioscience 53-4875; 1:400), Ctip2 (Abcam 18465; 1:300), Satb2 (Abcam 34735; 1:300). Sections were then incubated with fluorochrome-conjugated secondary antibodies (Life Technologies) for 2h at room temperature. All samples were counterstained with 1 $\mu\text{g}/\text{mL}$  DAPI in PBS, and mounted in Vectashield (Vector lab).

## 4.3 Image acquisition and quantification

Optical sections (1  $\mu\text{m}$  thick) of dorsal telencephalon (Fig 2B) were captured at 1024 density using 20x objective and 2x zoom function on a Leica confocal microscope (TCS SP5 AOBS). Cell nuclei were counted manually on a window of 387.5  $\mu\text{m}$  of width whose height varies according to the thickness of the cortex. For illustration, confocal images were cropped and adjusted for contrast by using Fiji and then arranged by FigureJ (plugin in Fiji) and InDesign adobe CS6.

## 4.4 Numerical method

The numerical method used to compute the solution of equations (1-2) is based on the method of characteristics. We can solve the PDEs (1) analytically through the characteristic curves:

$$\left\{ \begin{array}{l} IPP(t, 0) = \gamma(t)\beta(t)F_{AP}(t) \\ IPP(t, a) = \begin{cases} IPP(0, a-t) \text{ for } t < a < T_C^{IPP} \\ IPP(t-a, 0) \text{ for } 0 < a < t \end{cases} \\ IPN(t, 0) = (1-\gamma(t))\beta(t)F_{AP}(t) + 2IPP(t, T_C^{IPP}) \\ IPN(t, a) = \begin{cases} IPN(0, a-t) \text{ for } t < a < T_C^{IPN} \\ IPN(t-a, 0) \text{ for } 0 < a < t \end{cases} \end{array} \right. \quad (22)$$

The numerical method involves the discretization of (22) in age (space) and time. The space step  $\Delta_a$  is chosen so that there is an integer number of meshes,  $N_a$ , within the IPP cell cycle. Since the duration of

the IPN cell cycle is smaller than that of the IPN cycle ( $T_C^{IPP} > T_C^{IPN}$ ), not only the number of meshes  $\tilde{N}_a$  is different ( $\tilde{N}_a < N_a$ ), but also the latest mesh may be reduced in size:

$$\begin{aligned} T_C^{IPP} &= N_a \Delta_a, \quad \text{with } N_a \in \mathbb{N}. \\ T_C^{IPN} &= (\tilde{N}_a - (1 - \tilde{\delta})) \Delta_a, \quad \text{with } \tilde{N}_a \in \mathbb{N} \text{ and } 0 \leq \tilde{\delta} < 1, \end{aligned}$$

The time step is chosen to be equal to the space step:

$$\Delta := \Delta_t = \Delta_a.$$

The pseudo-code in Algorithm 1 describes how to compute the discretized cell densities  $IPP_j^n$  (respectively  $IPN_j^n$ ) of IPP (respectively IPN) at times  $n\Delta$  and ages  $j\Delta$

$$IPP_j^n \approx IPP(n\Delta, j\delta), \quad IPN_j^n \approx IPN(n\Delta, j\delta),$$

and how to integrate the densities over the whole domain to obtain the cell numbers, which are approximated by an order 2 quadrature.

```

for  $j = 1, \dots, N_a$  do
  |  $IPP_j^0 = IPP^0(j\Delta)$ 
end
for  $j = 1, \dots, \tilde{N}_a - 1$  do
  |  $IPN_j^0 = IPN^0(j\Delta)$ 
end
 $IPN_{\tilde{N}_a}^0 = IPN^0(T_C^N)$ 
for  $n = 1, 2, \dots$  do
  | for  $j = 1, \dots, N_a$  do
  | |  $IPP_j^n = IPP_{j-1}^{n-1}$ 
  | end
  |  $IPP_0^n = \gamma^n \beta^n F_{AP}^n$ 
  |  $IPN_0^n = (1 - \gamma^n) \beta^n F_{AP}^n + 2IPP_{N_a}^n$ 
  | for  $j = 1, \dots, \tilde{N}_a - 1$  do
  | |  $IPN_j^n = IPN_{j-1}^{n-1}$ 
  | end
  |  $IPN_{\tilde{N}_a}^n = \tilde{\delta} IPN_{\tilde{N}_a-2}^{n-1} + (1 - \tilde{\delta}) IPN_{\tilde{N}_a-1}^{n-1}$ 
  |  $\overline{IPP}^n = \frac{\Delta}{2} \left( IPP_0^n + 2 \sum_{i=1}^{N_a-1} IPP_i^n + IPP_{N_a}^n \right)$ 
  |  $\overline{IPN}^n = \frac{\Delta}{2} \left( IPN_0^n + 2 \sum_{i=1}^{\tilde{N}_a-2} IPN_i^n + (2 - \tilde{\delta}) IPN_{\tilde{N}_a-1}^n + (1 - \tilde{\delta}) IPN_{\tilde{N}_a}^n \right)$ 
end

```

**Algorithm 1:** Numerical algorithm used to compute the cell densities and total cell numbers of intermediate progenitors IPPs and IPNs. Partial cell numbers in M and S phases are obtained similarly; the values on the internal boundaries delimitating each phase are interpolated using the two nearest nodes. The corresponding python code CEMONE can be downloaded from <https://github.com/letsop/cemone>

## 4.5 Computation of the number of double labeled cells in S phase-labeling experiments

The approximated number of double labeled cells, mimicking the experimental result and entering equation 21, can be computed from extracting the contribution of Brdu labeled IPP cells to the number of IPN in S phase at time  $t_2$ ,

$$\overline{IPN}_S(t_2) = \int_{T_{G1}^{IPN}}^{T_{G1}^{IPN} + T_S^{IPN}} IPN(t_2, a) da. \quad (23)$$

According to the specific choice of  $t_2 - t_1$ , this quantity can be a mixture of:

1. Former IPP cells that were in S phase at  $t_1$ , corresponding to cells already labeled with BrdU;
2. Former IPP cells that were outside S phase at  $t_1$ , i.e. that had either overcome S phase (and were in M or G2 phase) or were still in G1 phase;
3. Former AP cells that divided within the  $[t_1, t_2]$  time interval and have reached phase S since then.

To stick to the experimental values and select only BrdU labeled cells within this mixture, we have to get rid of cells in case 2 or 3.

The common point between the three cell sources is that cells have entered a new IPN cell cycle in the interval  $\tau \in [t_2 - T_{G1}^{IPN} - T_S^{IPN}, t_2 - T_{G1}^{IPN}]$ , with the lower bound corresponding to cells at the very end of S phase, and the upper bound to cells at the very beginning of phase S. An alternative way to compute  $\overline{IPN}_S(t_2)$  in eq. (23) is thus to integrate boundary condition (2) in time along this interval :

$$\overline{IPN}_S(t_2) = \int_{t_2 - T_S^{IPN} - T_{G1}^{IPN}}^{t_2 - T_{G1}^{IPN}} \left\{ (1 - \gamma(\tau))\beta(\tau)F_{AP}(\tau) + 2IPP(\tau, T_c^{IPP}) \right\} d\tau. \quad (24)$$

To extract the contribution of the proper cells (case 1) from (24), we first get rid of the contribution of AP cells, which is straightforward.

For IPPs, things are a little more tricky. At any time  $\tau$  in eq. (24), IPPs contributing to  $\overline{IPN}_S(t_2)$  are aged  $T_c^{IPP}$ , meaning that they were aged  $T_c^{IPP} - (\tau - t_1)$  at time  $t_1$ . Hence we should keep only those cells whose age  $T_c^{IPP} - (\tau - t_1)$  at time  $t_1$  is compatible with their belonging to phase S at time, i.e. :

$$\begin{aligned} T_{G1}^{IPP} &\leq T_c^{IPP} - (\tau - t_1) \leq T_{G1}^{IPP} + T_S^{IPP}, \\ t_1 + T_c^{IPP} - T_{G1}^{IPP} - T_S^{IPP} &\leq \tau \leq t_1 + T_c^{IPP} - T_{G1}^{IPP}. \end{aligned}$$

Hence, the estimated number of double labeled cells at  $t_2$  is given by

$$\overline{IPN}_S^*(t_2) = \int_{\max(t_2 - T_S^{IPN} - T_{G1}^{IPN}; t_1 + T_c^{IPP} - T_{G1}^{IPP} - T_S^{IPP})}^{\min(t_2 - T_{G1}^{IPN}; t_1 + T_c^{IPP} - T_{G1}^{IPP})} 2IPP(\tau, T_c^{IPP}) d\tau, \quad (25)$$

or equivalently

$$\overline{IPN}_S^*(t_2) = \int_{\max(t_2 - T_S^{IPN} - T_{G1}^{IPN}; t_1 + T_{G2}^{IPP} + T_M^{IPP} + T_S^{IPP})}^{\min(t_2 - T_{G1}^{IPN}; t_1 + T_{G2}^{IPP} + T_M^{IPP} + T_S^{IPP})} 2IPP(\tau, T_c^{IPP}) d\tau.$$

Note that, since  $T_c^{IPP} - (\tau - t_1)$  can be rewritten as  $T_c^{IPP} - [(t_2 - t_1) - (t_2 - \tau)]$  this amounts to:

$$\begin{aligned} T_c^{IPP} - (T_{G1}^{IPP} + T_S^{IPP}) &\leq (t_2 - t_1) - (t_2 - \tau) \leq T_c^{IPP} - T_{G1}^{IPP} \\ T_{G2}^{IPP} + T_M^{IPP} &\leq (t_2 - t_1) - (t_2 - \tau) \leq T_{G2}^{IPP} + T_M^{IPP} + T_S^{IPP}. \end{aligned}$$

In the case when  $\tau = t_2 - T_{G1}^{IPN} - T_S^{IPN}$ , then

$$T_{G2}^{IPP} + T_M^{IPP} + T_{G1}^{IPN} + T_S^{IPN} \leq (t_2 - t_1) \leq T_{G2}^{IPP} + T_M^{IPP} + T_{G1}^{IPN} + T_S^{IPN} + T_S^{IPP}.$$

In the case when  $\tau = t_2 - T_{G1}^{IPN}$ , then

$$T_{G2}^{IPP} + T_M^{IPP} + T_{G1}^{IPN} \leq (t_2 - t_1) \leq T_{G2}^{IPP} + T_M^{IPP} + T_{G1}^{IPN} + T_S^{IPP}.$$

Hence, to make sure to detect at least some of the cells labeled by BrdU at  $t_1$  (hence to get less than 100 % false positive cells), the delay  $t_2 - t_1$  has to be bounded by

$$T_{G2}^{IPP} + T_M^{IPP} + T_{G1}^{IPN} \leq (t_2 - t_1) \leq T_{G2}^{IPP} + T_M^{IPP} + T_{G1}^{IPN} + T_S^{IPN} + T_S^{IPP}. \quad (26)$$

## 5 Discussion

We have undertaken an interdisciplinary approach to study the dynamics of neurogenesis in the developing mammalian cerebral cortex. Our work combines an experimental quantitative analysis of cell populations along the neurogenesis process in the mouse cortex, with mathematical modeling, numerical simulation and parameter optimization. The main results of this work are the following:

- We have built a compartmental model, which not only accounts for the temporal changes in cell numbers, but also embeds a multiscale description of the IP dynamics. IP cells can be tracked along the cell cycle as they progress into the subsequent cell phases until division, and quantitative information is available at the same time on several scales.
- Our formalism provides one with a framework to study how progenitor numbers, division modes and proliferation rates interact to control quantitatively and temporally the neuronal output.
- We successfully adjusted the model parameters to our experimental data on neurogenesis in the developing murine cerebral cortex in control conditions, which has enabled us to predict progenitor dynamics in a mutant context.
- We show how to compute cell kinetics indexes from the model outputs and to optimize experimental protocols intending to discriminate the different progenitor types.
- The model can be used in a straightforward manner to study other mouse mutants with cortical neurogenesis defects in a dedicated simulation environment (CEMONE).

So far, modeling approaches of cell lineage dynamics during the development of the cerebral cortex in embryos have been mainly undergone in the framework of the branching process formalism (see e.g. [13, 21, 24, 30]). In general, these approaches focus on the impact of division types (self-amplifying, self-renewing or self-consuming, following the terminology proposed in [11]) ; apoptosis can also be considered in studies with a background motivation of developmental toxicology [13, 19]. Such approaches can lead to interesting theoretical results on the properties of the population growth regime [24] or the cell lineage trees (size and degree of imbalance) [30]. Most of the time, the notion of progenitor cell is quite generic, and has no clear histological counterpart, except in some cases where model cell types can be mapped to biological cell types [21]. When it exists, the confrontation of the model outputs to experimental data remains on an average, whole population level. This is due to the fact that the natural time increment in these models is expressed as the cell generation number, which is hardly interpretable as a physical time unit. To circumvent this problem and relate the generation number with physical time (and specifically with embryonic day units), one needs to apply simplifying assumptions on the cell cycle duration (considered as constant over all cell types as well as over time) and transit times all along the cell cycle (stationary uniform distribution of cells within the cell cycle).

Another approach focused, as we do here, on the dynamics of intermediate progenitors, to explain compensation for neuron loss, as well as different neuron distribution into upper or deeper layers, in *Dbx1*-deleted transgenic mice [12]. Through stochastic simulations based on the Gillespie algorithm, the authors investigated the possible impact of several IPgenic divisions, and alteration in IP cell cycle duration. Yet, in contrast to the present work, their stochastic compartmental model does not account for the structuring of IP cell cycles into phases G1, S, G2 and M, and, more importantly, the simulated model outputs remain theoretical, to the extent that they did not compare the model outputs to quantitative experimental data. In contrast, we put a great effort on the acquisition of both quantitative and kinetics data on IP and neuron cell numbers and optimization of the model parameters with respect to the changes in the experimental cell numbers.

Even if adult neurogenesis is very different from developmental neurogenesis, especially as for the involvement of apoptosis in non pathological situations, we also mention here some recent works dealing with adult hippocampal neurogenesis. In particular, in [20], the authors introduced a multitype Bellman-Harris branching process, which explicitly takes into account the cell cycle phases and generation number



of amplifying neuroprogenitors. They took advantage of the stationary nature of adult neurogenesis on the short term to obtain experimentally plausible cell numbers (from raw data expressed as proportion of BrdU labeled cell types). In contrast, the motivation of [35,36] was mainly to explain the long term decay in the hippocampal pool of neural stem cells, by means of a deterministic compartmental model and its stochastic counterpart with similar average transit times (hence cell cycle durations) within each compartment.

In our approach, the model assumptions are based on state-of-the-art knowledge on cortex cell dynamics during development [1,17] as far as (i) identification of cell types (distinction between APs and IPs, and further between IPPs and IPNs), (ii) cell flows between cell populations (neurogenic versus IP-genic division in APs and IPs), as well as between-type differences in cell cycle and cell phase durations. In addition to giving a good fit with experimental IP and neuron cell numbers, the model output also predicts trends in the neurogenic fraction that are consistent with the detailed results provided in [17], which corroborates the very low (and possibly neglectable) direct neurogenesis rate from APs ( $\beta(t)$ ) and the formulation of the time-dependence of proliferative IP production ( $\gamma(t)$ ).

One can easily use our framework to study other experimental situations in rodents. The quantitative effect of changing some parameter values can be tested and visualized in a user-friendly and interactive manner in the CEMONE environment (ipython notebook). The structure of the model could also be further adapted to take into account other populations of progenitors and neurons, in the cortex or even in other regions of the central nervous system. Two important adaptations could be made. First, an important improvement would be to take into account the number and cell cycle length of APs. This would require to be able to quantify APs engaged in neurogenesis, for instance by using the Tis21-GFP transgenic mouse line [16]. Second, in the cerebral cortex, different types of neurons are produced in a precise temporal order and form six major neuronal layers with distinct properties, connectivity and molecular signatures, that can be fully identified after birth [14,22,27]. Our model could be adapted to study the temporal dynamics of neuronal subtype production.

Our model can be also adapted to study the importance of progenitor dynamics on cortical evolution and disease. IPs in mice have limited proliferation potential, and it has been proposed that an increase in this potential participates in the tremendous brain growth size in primates. An increased proliferation potential of IPs (i.e. the possibility that each IPP makes more than two divisions) could be easily implemented in the model. In addition, other types of progenitors can be introduced with different cell cycle rates, division modes and proliferation potential, such as outer radial glial cells, which are also proposed to contribute to the increase in cortical size during mammalian brain evolution. The adaptation of our model to investigate human cortical neurogenesis would also be of great interest for understanding neurodevelopmental diseases.

## 6 Acknowledgements

This work was funded by the Agence Nationale pour la Recherche (ANR blanc “CILIAINTHEBRAIN”, project 11-BSV2-0006 to S.S.M.), the Fondation pour la Recherche Médicale (Equipe FRM DEQ20140329544 to S.S.M.), the “Association pour la Recherche sur le Cancer” (ARC, PJA 20171206591 grant to S.S.M.) and Sorbonne Universités (Idex Super Emergence Program, project “NeuroMathMod” SU-15-R-EMR-05 to M.P.). We thank the imaging platform of the IBPS for assistance with microscopy, the IBPS mouse facility for animal care, Sophie Gournet for help in the illustrations, and Marie Breau, Christine Vesque and Danielle Monniaux for critical reading of the manuscript.

## References

- [1] Y. Arai, J.N. Pulvers, C Haffner, B. Schilling, I. Nusslein, F. Calegari, and W.B. Huttner. Neural stem and progenitor cells shorten S-phase on commitment to neuron production. *Nat. Commun.*,

2:154, 2011.

- [2] Paola Arlotta, Bradley J. Molyneaux, Jinhui Chen, Jun Inoue, Ryo Kominami, and Jeffrey D. Macklis. Neuronal subtype-specific genes that control corticospinal motor neuron development in vivo. *Neuron*, 45(2):207–221, 2004.
- [3] A. Attardo, F. Calegari, W. Haubensak, M. Wilsch-Braüninger, and W.B. Huttner. Live imaging at the onset of cortical neurogenesis reveals differential appearance of the neuronal phenotype in apical versus basal progenitor progeny. *PLoS One*, 3(6):e2388, 2015.
- [4] B. Aymard, F. Clément, D. Monniaux, and M. Postel. Cell-kinetics based calibration of a multiscale model of structured cell populations in ovarian follicles. *SIAM J. Appl. Math.*, 76(4):1471–1491, 2016.
- [5] K. Baker and PL. Beales. Making sense of cilia in disease: the human ciliopathies. *Am. J. Med. Genet. C Semin. Med. Genet.*, 151C(281), 2009.
- [6] Laurianne Besse, Mariame Neti, Isabelle Anselme, Christoph Gerhardt, Ulrich Rütter, Christine Laclef, and Sylvie Schneider-Maunoury. Primary cilia control telencephalic patterning and morphogenesis via gli3 proteolytic processing. *Development*, 138(10):2079–2088, 2011.
- [7] M. Betizeau, V. Cortay, D. Patti, S. Pfister, E. Gautier, A. Bellemin-Ménard, M. Afanassieff, C. Huisoud, R.J. Douglas, H. Kennedy, and C. Dehay. Precursor diversity and complexity of lineage relationships in the outer subventricular zone of the primate. *Neuron*, 80(2):442 – 457, 2013.
- [8] Olga Britanova, Camino de Juan Romero, Amanda Cheung, Kenneth Y. Kwan, Andrea Schwark, Manuelaand Gyorgy, Tanja Vogel, Sergey Akopov, Mišo Mitkovski, Denes Agoston, et al. *Satb2* is a postmitotic determinant for upper-layer neuron specification in the neocortex. *Neuron*, 57(3):378–392, 2008.
- [9] Marion Delous, Lekbir Baala, Rémi Salomon, Christine Laclef, Jeanette Vierkotten, Kàlmàn Tory, Christelle Golzio, Tiphonie Lacoste, Laurianne Besse, Catherine Ozilou, et al. The ciliary gene *rp-grip11* is mutated in cerebello-oculo-renal syndrome (joubert syndrome type b) and meckel syndrome. *Nature genetics*, 39(7):875, 2007.
- [10] C. Englund, A. Fink, C. Lau, D. Pham, R.A. Daza, A. Bulfone, T. Kowalczyk, and R.F. Hevner. *Pax6*, *tbr2*, and *tbr1* are expressed sequentially by radial glia, intermediate progenitor cells, and postmitotic neurons in developing neocortex. *J. Neurosci.*, 25(1):247–251, 2005.
- [11] M. Florio and W.B. Huttner. Neural progenitors, neurogenesis and the evolution of the neocortex. *Development*, 141(11):2182–2194, 2014.
- [12] Betty Freret-Hodara, Yi Cui, Amélie Griveau, Lisa Vigier, Yoko Arai, Jonathan Touboul, and Alessandra Pierani. Enhanced abventricular proliferation compensates cell death in the embryonic cerebral cortex. *Cereb. Cortex*, pages 1–18, 2016.
- [13] Julia M. Gohlke, William C. Griffith, and Elaine M. Faustman. Computational models of neocortical neuronogenesis and programmed cell death in the developing mouse, monkey, and human. *Cereb. Cortex*, 17(10):2433–2442, 2007.
- [14] Luciano Custo Greig, Mollie B Woodworth, Maria J Galazo, Hari Padmanabhan, and Jeffrey D Macklis. Molecular logic of neocortical projection neuron specification, development and diversity. *Nat. Rev. Neurosci.*, 14(11):755–769, 2013.
- [15] N. Hansen, S.D. Müller, and P. Koumoutsakos. Reducing the time complexity of the derandomized evolution strategy with covariance matrix adaptation (cma-es). *Evol. Comput.*, 11(1):1–18, 2003.
- [16] W. Haubensak, A. Attardo, W. Denk, and W.B. Huttner. Neurons arise in the basal neuroepithelium of the early mammalian telencephalon: A major site of neurogenesis. *Proc. Natl. Acad. Sci. U.S.A.*, 101(9):3196–3201, 2004.

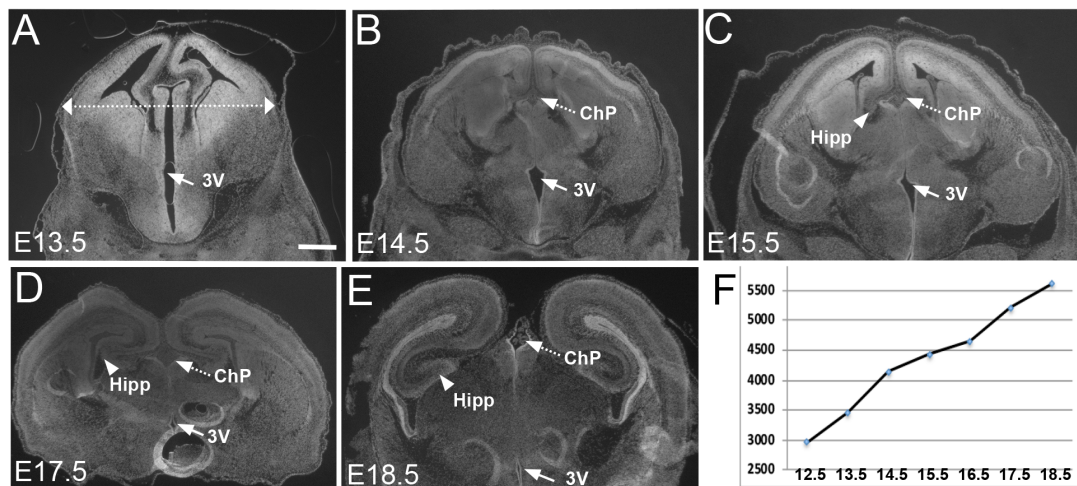
- [17] T. Kowalczyk, A. Pontious, C. Englund, R.A.M. Daza, F. Bedogni, R. Hodge, A. Attardo, C. Bell, W.B. Huttner, and R.F. Hevner. Intermediate neuronal progenitors (basal progenitors) produce pyramidal projection neurons for all layers of cerebral cortex. *Cereb. Cortex*, 19(10):2439–2450, 2009.
- [18] J.E. Lee and J.G. Gleeson. Cilia in the nervous system: linking cilia function and neurodevelopmental disorders. *Curr. Opin. Neurol.*, 24(2):98–105, 2011.
- [19] B.G. Leroux, W.M. Leisenring, S.H. Moolgavkar, and E.M. Faustman. A biologically-based dose response model for developmental toxicology. *Risk Anal.*, 16(4):449–458, 1996.
- [20] B. Li, A. Sierra, J.J. Deudero, F. Semerci, M Laitman, A. and Kimmel, and M. Maletic-Savatic. Multitype bellman-harris branching model provides biological predictors of early stages of adult hippocampal neurogenesis. *BMC Syst. Biol.*, 11(5):90, 2017.
- [21] H.R. MacMillan and M.J. McConnell. Seeing beyond the average cell: branching process models of cell proliferation, differentiation, and death during mouse brain development. *Theory Biosci.*, 130(1):31–43, 2011.
- [22] Martine N. Manuel, Da Mi, John O. Mason, and David J. Price. Regulation of cerebral cortical neurogenesis by the pax6 transcription factor. *Front Cell Neurosci*, 9:70, 2015.
- [23] B. Martynoga, H. Morrison, D.J. Price, and J.O Mason. Foxg1 is required for specification of ventral telencephalon and region-specific regulation of dorsal telencephalic precursor proliferation and apoptosis. *Dev. Biol.*, 283(1):113–127, 2005.
- [24] D.G. Míguez. A branching process to characterize the dynamics of stem cell differentiation. *Sci. Rep.*, 19(5):13265, 2015.
- [25] F.D. Miller and A.S. Gauthier. Timing is everything: making neurons versus glia in the developing cortex. *Neuron*, 54:357–369, 2007.
- [26] T. Miyata, A. Kawaguchi, K. Saito, M. Kawano, T. Muto, and M. Ogawa. Asymmetric production of surface-dividing and non-surface-dividing cortical progenitor cells. *Development*, 131:3133–3145, 2004.
- [27] B.J. Molyneaux, P. Arlotta, J.R. Menezes, and J.D. Macklis. Neuronal subtype specification in the cerebral cortex. *Nat. Rev. Neurosci.*, 8(427), 2007.
- [28] S.C. Noctor, V. Martínez-Cerdeño, L. Ivic, and A.R. Kriegstein. Cortical neurons arise in symmetric and asymmetric division zones and migrate through specific phases. *Nature Neurosci.*, 7(2):136–144, 2004.
- [29] M. Okamoto, T. Namba, T. Shinoda, T. Kondo, T. Watanabe, Y. Inoue, K. Takeuchi, Y. Enomoto, K. Ota, K. Oda, Y. Wada, K. Sagou, K. Saito, A. Sakakibara, A. Kawaguchi, K. Nakajima, T. Adachi, T. Fujimori, M. Ueda, S. Hayashi, K. Kaibuchi, and T. Miyata. TAG-1-assisted progenitor elongation streamlines nuclear migration to optimize subapical crowding. *Nat. Neurosci.*, 16(11):1556–1566, 2013.
- [30] J.L. Slater, K.A. Landman, B.D. Hughes, Q. Shen, and S. Temple. Cell lineage tree models of neurogenesis. *J. Theor. Biol.*, 256(2):164 – 179, 2009.
- [31] H. Tabata. Diverse subtypes of astrocytes and their development during corticogenesis. *Frontiers Neurosci.*, 9(114):1–7, 2015.
- [32] Jeanette Vierkotten, Renate Dildrop, Thomas Peters, Baolin Wang, and Ulrich Rütter. Ftm is a novel basal body protein of cilia involved in shh signalling. *Development*, 134(14):2569–2577, 2007.
- [33] L. Wang, S. Hou, and Han Y.G. Hedgehog signaling promotes basal progenitor expansion and the growth and folding of the neocortex. *Nat. Neurosci.*, 19(7):888–96, 2016.

- [34] Fong Kuan Wong, Ji-Feng Fei, Felipe Mora-Bermúdez, Elena Taverna, Christiane Haffner, Jun Fu, Konstantinos Anastasiadis, A Francis Stewart, and Wieland B Huttner. Sustained pax6 expression generates primate-like basal radial glia in developing mouse neocortex. *PLoS Biol.*, 13(8):e1002217, 2015.
- [35] F. Ziebell, S. Dehler, A. Martin-Villalba, and A. Marciniak-Czochra. Revealing age-related changes of adult hippocampal neurogenesis using mathematical models. *Development*, 145(1), 2018.
- [36] F. Ziebell, A. Martin-Villalba, and A. Marciniak-Czochra. Mathematical modelling of adult hippocampal neurogenesis: effects of altered stem cell dynamics on cell counts and bromodeoxyuridine-labelled cells. *J. Royal Soc. Interface*, 11(94), 2014.

## A Supporting Information

### S1 Fig

**Histological and morphometric criteria used for staging control brain sections.** A-E) Representative pictures of brain sections from control embryos used in this study. The dotted double arrow in A shows the width of the brain section. Full arrows point to the ventral part of the third ventricle (3V); dotted arrows point to the choroid plexus (ChP) present in the dorsal part of 3V from E14.5 onward; arrowheads point to the hippocampus (Hipp), showing its progressive folding. F) Graph illustrating the linear progression of brain width with the embryonic stage, using reference sections taken from the Allen Atlas of the developing mouse brain (<http://developingmouse.brain-map.org/static/atlas>).



## S1 Table

### Notations and terminology used in the paper

Notation	Definition	Description
AP	Apical progenitor	
IP	Intermediate progenitor	
N	Neuron	
IPN	Neurogenic IP	IP that divides symmetrically to give two Ns
IPP	Proliferative / IPgenic IP	IP that divides symmetrically to give rise to two IPNs
$F_{AP}(t)$	AP inflow into neurogenesis	Instantaneous AP Number fuelling neurogenesis
$K_{AP}$	Parameters of $F_{AP}(t)$ formulated in (eq. 11)	Scaling factor
$t^+$		Location of the rise inflexion point
$s^+$		The slope of $F_{AP}(t)$ at $t^+$ is approximately $4s^+K_{AP}$
$t^-$		Location of the decay inflexion point
$s^-$		The slope of $F_{AP}(t)$ at $t^-$ is approximately $-4s^-K_{AP}$
$\beta(t)$	Ratio of IP-genic divisions of APs	Proportion of fated AP subject to direct neurogenesis
$\gamma(t)$	Ratio of IPP-genic AP divisions	Proportion of fated AP subject to an IPgenic division entering an IPP cell cycle
$\gamma_0$	Parameters of $\gamma(t)$ formulated in a sigmoid (eq. 10)	Limit value of $\gamma(t)$ for $t \rightarrow -\infty$
$\gamma_1$		Limit value of $\gamma(t)$ for $t \rightarrow +\infty$
$t_\gamma$		Location of inflexion point of $\gamma(t)$
$s_\gamma$		$4s_\gamma/(\gamma_1 - \gamma_0)$ is the slope of $\gamma(t)$ at $t_\gamma$
$X(t, a)$	Density of cells at time $t$ and age $a$	Density of cells of type $X \in \{\text{IPP}, \text{IPN}\}$ , solution of PDE (eq. 1)
$\bar{X}(t)$	Number of cells of type X	Number of cells X at time $t$ . $X \in \{\text{IPP}, \text{IPN}, \text{IP}, \text{N}\}$
$a$	age	Location within the cell cycle
$\bar{X}_P(t)$	X in the $P$ phase	$X \in \{\text{IPP}, \text{IPN}, \text{IP}\}$ ; $P \in \{G1, S, G2, M\}$
$LI(t)$	Labeling index (eq. 8)	Proportion of cells in $S$ phase over the total number of cycling cells (defined for a specific progenitor type)
$MI(t)$	Mitotic index (eq. 9)	Proportion of cells in $M$ phase over the total number of cycling cells (defined for a specific progenitor type)
$\psi(t)$	IP neurogenic fraction (eq. 7)	Proportion of IP mitoses fated to neurogenic divisions
$\rho(t, \Delta t)$	Proportion of IP cells in S phase at $t$ and $t + \Delta t$ detected by double labeling (eq. 21)	Efficiency of detection of cells undergoing a second S phase by double-labeling techniques based on a large delay $\Delta t$
$r_{AP}^N$	Neuronal yield (eq. 15)	Ratio of the final number of produced neurons over the cumulated number of AP that have entered neurogenesis

## S2 Table

**Durations of the IPP and IPN cell cycle phases at E14.5**, taken from Arai et al. [1]. Time are given in hours (h).

	$T_C$	$T_S$	$T_{G2}$	$T_M$	$T_{G1}$
IPPs	29.4	6.4	1.6	0.5	20.9
IPNs	26.2	2.8	1.6	0.5	21.3

### S3 Table

Cell types and marker combinations used for their quantification.

Cortical cell	Stage	Marker combination	ref
Apical progenitors (APs)	E12.5-E18.5	Pax6 <sup>+</sup> , Tbr2 <sup>-</sup>	[10]
Intermediate progenitors (IPs)	E12.5-E18.5	Tbr2 <sup>+</sup> , Ctip2 <sup>-</sup>	[10]
Proliferative IPs (IPPs)	E12.5-E18.5	Pax6 <sup>+</sup> Tbr2 <sup>+</sup>	[34]
Neurons	E12.5	Ctip2 <sup>+</sup> , Tbr2 <sup>-</sup>	[2]
	E13.5-E18.5	(Ctip2 <sup>+</sup> , Satb2 <sup>-</sup> ) + (Ctip2 <sup>+</sup> , Satb2 <sup>+</sup> )	[8]



## S4 Table

**Cell counts.** Values in columns D, E and H correspond to the dots in Fig 4G, 4F and 4H. Lines labeled with Ctrl correspond to wild type (WT) in blue and Ftm-/- to (KO) mutant in red. Points at a given age correspond to different embryos, from up to two different litters.

		APs			Deep Layer (DL) neurons		Upper Layer (UL) neurons	Total neurons	
		Pax6+Tbr2-	IPPs Pax6+Tbr2+	IPs Tbr2+Ctip2-	Ctip2+	Satb2-	Satb2+	DL + UL	
E12.5	Ctrl	480	38	151	89		nd	89	
		499	38	142	97		nd	97	
		472	21	151	77		nd	77	
		404	48	127	81		nd	81	
		485	24	113	82		nd	82	
		500	15	154	85		nd	85	
		475	18	96	96		nd	96	
	486	24	127	127		nd	127		
	417	16	81	81		nd	81		
	409	8	84	38		nd	38		
	485	10	99	61		nd	61		
	378	4	35	53		nd	53		
	E13.5	Ctrl	658	73	378	52		159	211
			647	79	377	57		171	228
603			64	373	49		165	214	
509			64	239	56		174	230	
677			13	131	132		2	134	
401		16	133	127		0	127		
470		16	125	116		1	117		
466		10	112	153		6	159		
E14.5		Ctrl	607	99	490	132		546	678
			511	78	370	245		463	708
	576		74	436	186		531	717	
	413	61	234	93		41	134		
	467	70	293	78		113	191		
	464	54	307	77		139	216		
E15	Ctrl	458	51	396	154		560	714	
		507	53	347	143		575	718	
		554	128	394	268		189	457	
	449	73	295	548		249	797		
	508	143	378	279		411	690		
E15.5	Ctrl	458	143	486	220		1040	1260	
		459	120	406	265		730	995	
		414	106	390	250		950	1200	
	483	138	570	76		507	583		
	341	100	439	111		751	862		
	514	143	614	185		680	865		
E16	Ctrl	417	92	536	333		923	1256	
		372	127	452	366		820	1186	
		428	150	516	305		932	1237	
		610	214	734	219		716	935	
	592	254	684	189		382	571		
	564	225	611	205		594	799		
	E16.5	Ctrl	324	121	486	402		987	1389
210			93	337	415		973	1388	
274			103	375	407		969	1376	
312		171	501	182		1078	1260		
385		122	486	330		789	1119		
365		121	495	264		963	1227		
E17.5	Ctrl	435	103	420	151		938	1089	
		335	86	395	149		942	1091	
		337	87	404	155		953	1108	
	272	67	221	172		851	1023		
	268	98	282	167		845	1012		
E18.5	Ctrl	297	50	104	390		654	1044	
		282	57	96	380		748	1128	
		144	43	167	624		680	1304	
	109	8	150	635		714	1349		
	112	30	172	142		862	1004		